Journal of Rock Mechanics and Geotechnical Engineering 16 (2024) 1262–1279

Contents lists available at ScienceDirect

Journal of Rock Mechanics and Geotechnical Engineering

journal homepage: www.jrmge.cn

Full Length Article

Anisotropic time-dependent behaviors of shale under direct shearing and associated empirical creep models

Yachen Xie [a,b,c], Michael Z. Hou [b], Hejuan Liu [c], Cunbao Li [a,*]

[a] Shenzhen Key Laboratory of Deep Engineering Sciences and Green Energy, Shenzhen University, Shenzhen, 518060, China
[b] Institute of Subsurface Energy Systems, Clausthal University of Technology, Clausthal-Zellerfeld, 38678, Germany
[c] State Key Laboratory of Geomechanics and Geotechnical Engineering, Institute of Rock and Soil Mechanics, Chinese Academy of Sciences, Wuhan, 430071, China

ARTICLE INFO

Article history:
Received 12 February 2023
Received in revised form
15 April 2023
Accepted 30 May 2023
Available online 1 June 2023

Keywords:
Rock anisotropy
Direct shear creep
Creep compliance
Steady-creep rate
Empirical model
Creep constitutive model

ABSTRACT

Understanding the anisotropic creep behaviors of shale under direct shearing is a challenging issue. In this context, we conducted shear-creep and steady-creep tests on shale with five bedding orientations (i.e. 0°, 30°, 45°, 60°, and 90°), under multiple levels of direct shearing for the first time. The results show that the anisotropic creep of shale exhibits a significant stress-dependent behavior. Under a low shear stress, the creep compliance of shale increases linearly with the logarithm of time at all bedding orientations, and the increase depends on the bedding orientation and creep time. Under high shear stress conditions, the creep compliance of shale is minimal when the bedding orientation is 0°, and the steady-creep rate of shale increases significantly with increasing bedding orientations of 30°, 45°, 60°, and 90°. The stress-strain values corresponding to the inception of the accelerated creep stage show an increasing and then decreasing trend with the bedding orientation. A semilogarithmic model that could reflect the stress dependence of the steady-creep rate while considering the hardening and damage process is proposed. The model minimizes the deviation of the calculated steady-state creep rate from the observed value and reveals the behavior of the bedding orientation's influence on the steady-creep rate. The applicability of the five classical empirical creep models is quantitatively evaluated. It shows that the logarithmic model can well explain the experimental creep strain and creep rate, and it can accurately predict long-term shear creep deformation. Based on an improved logarithmic model, the variations in creep parameters with shear stress and bedding orientations are discussed. With abovementioned findings, a mathematical method for constructing an anisotropic shear creep model of shale is proposed, which can characterize the nonlinear dependence of the anisotropic shear creep behavior of shale on the bedding orientation.

1. Introduction

The technical innovation of hydraulic fracturing and horizontal drilling has made the exploitation of shale gas economically feasible (Bellani et al., 2021). In engineering practice, the key to achieve long-term and sustainable shale gas production is to maintain the long-term effectiveness of the reservoir fracture network. However, field data from shale gas wells in major shale gas reservoirs in USA (such as the Barnett, Fayetteville, Woodford, Haynesville, and Eagle Ford) show that shale gas production exhibits a noticeable decreasing trend after 6–8 months of production (Baihly et al., 2010; Li et al., 2019). One of the critical causes of this decrease is the gradual reduction in fracture width and decrease in reservoir fracture network permeability due to long-term creep (Rassouli and Zoback, 2018). From a rock mechanics perspective, the primary types of loads that cause creep are compressive/tensile stress and shear stress (Zhao et al., 2011; Guner et al., 2022). Studies show that shale gas reservoirs are subjected to shearing during and after reservoir stimulation (Palmer et al., 2007; McClure and Horne, 2014). This shear stress can induce more complex fracture networks during shale gas reservoir stimulation, and has a substantial impact on the closure of reservoir fractures, stability of wellbore (Carey et al., 2015), and accurate measurement of ground stress (Geng et al., 2017) due to its long-term effects such as creep (Sone and Zoback, 2014). In addition, the inherent

* Corresponding author.
E-mail address: cunbao.li@szu.edu.cn (C. Li).
Peer review under responsibility of Institute of Rock and Soil Mechanics, Chinese Academy of Sciences.

https://doi.org/10.1016/j.jrmge.2023.05.001

anisotropic properties of shale caused by bedding further complicate the anisotropic creep behavior of shale under shearing.

At present, few studies are reported on the anisotropic creep of shale under direct shearing. Most studies have used conventional uniaxial/triaxial compression creep tests to analyze the creep properties of shale (Geng et al., 2017; Trzeciak et al., 2018; Wilczynski et al., 2021). For example, Chang and Zoback (2009) found that shale exhibits significant viscous creep behavior under hydrostatic pressure and triaxial compression, and the creep deformation increases with increasing clay/organic matter content. Sone and Zoback (2013b), Yang and Zoback (2016), and Herrmann et al. (2020) obtained similar conclusions using similar experimental methods. Based on nano-indentation creep tests of shale, Slim et al. (2019), Shi et al. (2020), Du et al. (2021), and Liu et al. (2021b) found that shale samples rich in weak components (clay/organic matter) have significantly lower creep moduli than quartz-rich samples and thus a higher creep strain, suggesting that creep behavior depends on shale composition. Similar to the conventional rock creep properties, shale creep deformation increases significantly under water-saturated or high-temperature conditions (Liang et al., 2020; Wang et al., 2022b). Li et al. (2022) conducted graded unloading creep tests on shale samples with different water saturations and found that both creep deformation and creep rate increase with increasing water content. Rybacki et al. (2017) and Herrmann et al. (2020) studied the creep behavior of Posidonia shale and found that the temperature conditions related to the depth of the reservoir have a similar effect on shale creep deformation upon the changes in composition and water content. Furthermore, Voltolini (2021) revealed the microscopic mechanism of temperature-driven shale creep by in situ synchrotron X-ray micro-computed tomography (CT) scanning technology, and found that temperatures as low as 75 °C could lead to rapid creep, with significantly accelerated crack aperture closure velocity. Concerning the confining pressure dependence of shale creep, some studies (Kamali-Asl and Ghazanfari, 2017; Sone and Zoback, 2014) indicate a weak dependence on hydrostatic stress, while others (Chang and Zoback, 2009; Herrmann et al., 2020) show a direct dependence. Nevertheless, these studies only focus on the creep deformation behavior of shale under compressive loading, and it is difficult to explain the creep mechanism of shale under direct shear paths.

The above-mentioned studies ignore the impact of shale anisotropy on its creep deformation. Some studies (Geng et al., 2018; Traore et al., 2022) show that inherent anisotropy has significant influences on the mechanical behaviors, and the degree of anisotropy has a significant effect on the acceleration of creep. Most of the shale creep tests only consider bedding horizontal or vertical to loading. Li et al. (2020) conducted triaxial multistage compression creep tests on shale samples with four bedding orientations (0°, 45°, 75°, and 90°) for the first time and found that under the same shear stress conditions, the creep deformation and steady-state creep rate are maximized and minimized at bedding orientations of 45° and 90°, respectively. They proposed three different mechanisms of shale creep under various bedding orientations. This also proves that the creep behavior under shearing differs from that under compression, and it seems that the anisotropy resulting from bedding can significantly affect the creep behaviors (Li et al., 2019). However, the anisotropic creep behavior of shale under direct shear is rarely investigated.

The constitutive model serves as a bridge connecting fundamental theories, experimental data, and engineering practices (Li et al., 2017; Kong et al., 2023). To date, numerous scholars have proposed various constitutive equations based on different assumptions to characterize the creep behavior of rocks, which can be divided into three categories: empirical formula models, component combination models, and creep models based on plastic mechanics, damage mechanics, or endochronic theory (Li et al., 2017). Although the second and third types of creep models have more rigorous physical foundations, they involve numerous model parameters and cannot comprehensively address the complex mechanisms of the multiple microscopic deformation-related interactions during the creep process of bedded shale. This suggests that the proposed creep models may be impractical for engineering applications. In this case, empirical models are widely applied due to their simplicity and practicality. The power law function model has been suggested to describe the variation in creep deformation of shale over time in some experiments (Rassouli and Zoback, 2018; Herrmann et al., 2020; Wang et al., 2022a). Although the power law model can be used to describe stress corrosion at the contact between rock particles, which is not caused by frictional sliding or subcritical crack expansion, the power law function model cannot reflect the creep mechanism. Some studies (e.g. Mighani et al., 2019; Liu et al., 2021a) use the logarithmic function model to characterize the time-dependent properties of shale deformation; while some scholars (e.g. Chau et al., 2017; Mighani et al., 2019) believe that the creep behavior of shale under different stresses and temperatures is a statistical behavior represented by a logarithmic function, which may be attributed to the significant number of displacement activation points commonly observed in rock creep. Other scholars (e.g. Hilsdorf and Müller, 1983; De Schutter, 1999) have also proposed exponential or hyperbolic function empirical constitutive equations for creep, assuming the existence of a bounded creep threshold. Microscopic research on rock creep has shown that the macroscopic time-dependent behavior of rocks is closely related to the time-dependent process of microscopic (grain size) crack propagation, based on which Brantut et al. (2014) proposed an empirical creep equation considering the damage evolution function of cracks. The commonly used empirical creep models can approximately describe creep deformations occurring within a few hours to a few weeks. However, these models are primarily applied to characterize creep deformations under compressive loading paths, and their capability to describe creep properties under shear loading needs to be investigated. Moreover, few of the existing models consider the effect of anisotropy on the predictive capability of the models.

To analyze the anisotropic creep behaviors of shale under direct shear and to identify more reasonable creep models for predicting the long-term shear mechanical behaviors of shale, this study conducts anisotropic creep tests on shale samples with five bedding inclinations (0°, 30°, 45°, 60°, 90°) under different levels of direct shear stress. In addition, an empirical model is proposed that improves some shortcomings of previous empirical models and can better characterize the shear creep behavior of shale. Based on the proposed empirical model, a mathematical method for constructing a reliable anisotropic shear creep model for shale is presented.

2. Shale creep test scheme under direct shearing

2.1. Specimen preparation and experimental set-up

All the shale samples used in this study were obtained from the same unweathered and intact outcrop of the lower Silurian Longmaxi Formation, Chongqing, China. The outcrop exposes dark brown carbonaceous shale with a dry density of approximately 2640 kg/m^3, a porosity of approximately 5%, and an apparent laminated structure. An X-ray diffraction analysis (Li et al., 2020, 2023) showed that the mineral composition of this shale is quartz (approximately 37 wt% by weight), clay (approximately 34.2 wt%), and carbonates (approximately 13 wt%). The shale outcrop materials were preserved in several layers by polyvinyl chloride (PVC) film to prevent it from weathering. The outcrop shale was finely

lathed, with compressed air as the cooling fluid to produce cubic specimens with five bedding inclinations ($\alpha = 0°$, 30°, 45°, 60°, and 90°). The bedding inclination α is defined as the angle between the bedding plane and the predetermined shear failure plane, as shown in Fig. 1a. The side length of the cubic samples was 50 mm. The surface flatness of the six faces of each cubic specimen was within ±0.02 mm. The front and back, top and bottom, and left and right faces of the specimens were parallel to each other, and any two adjacent faces were perpendicular to each other (see Fig. 1b). In addition, to reduce the error caused by the dispersion of the specimens, the processed shale specimens were measured by ultrasonic waves, and specimens with similar longitudinal wave velocities were selected for creep testing.

The creep tests were conducted using the rock shear test system developed by Sichuan University, China, as shown in Fig. 2. The test system features high axial and horizontal stiffness, high accuracy and reliable performance, with a maximum axial load of 1000 kN and a maximum horizontal load of 2500 kN. The vertical and shear deformations were measured by two linear variable displacement transducers (LVDTs), with a deformability measurement range of ±3 mm and a measurement accuracy of ±1 μm. This system could continuously record the deformation and stress data of the sample during the experiment at a maximum acquisition frequency of 5 Hz.

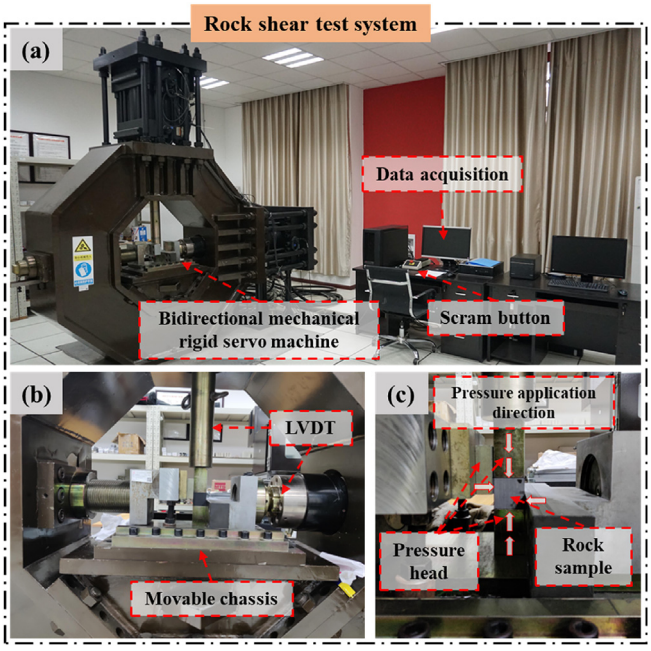

Fig. 2. Rock shear mechanics testing system: (a) Layout of the entire test system; (b) A close shot of the bidirectional rigid servo machine; and (c) Specimen installation and pressure application direction.

2.2. Experimental methodology

To simulate the geologic conditions, the normal stress σ_n was set to 30 MPa. Three direct shear tests were conducted on shale specimens with 5 different bedding inclinations to ascertain the multiple levels of direct shear creep stress. Fan et al. (2022) showed that the crack initiation stress of shale under a direct shearing path is generally 40% of its shear strength approximately. Thus, in this paper, the first level of shear creep stress in the shear creep test was 50% of the average shear strength of the shale for each bedding orientation, and then the creep stress was increased at a rate of 10% for subsequent stress levels until failure of the specimen. The shear stress path is shown in Fig. 3. First, the normal stress was loaded to the design stress level σ_n at a constant rate of 4.8 MPa/min and then maintained constant; and then, the first level of shear load τ_a was applied at a constant rate of 4 MPa/min. A 24-h creep test is considered to be sufficient for understanding the long-term mechanical behavior of shale (Wang et al., 2022a). Therefore, a constant shear stress was applied for 48 h, and the shear creep was recorded during this time period. If the specimens did not show failure under the current shear stress level for more than 48 h, the shear stress was increased to the next level and maintained for another 48 h. The above steps were repeated until failure of the tested specimen. Table 1 lists the shear stress values corresponding to the shear-creep stress path under different bedding orientations. Furthermore, to obtain the elasto-viscoplastic creep properties (Zhao et al., 2017) of shale under shear stress conditions, unloading shear creep tests are also conducted on shale specimens with bedding inclinations of 30° and 60°, and the relevant shear stress paths are shown in Fig. 3. In all of the shear creep tests, the vertical compressive load, vertical compressive displacement, horizontal shear load, and shear displacement were measured. All tests were conducted in a laboratory with a constant temperature (25 °C) to eliminate the thermal effect on the creep behavior.

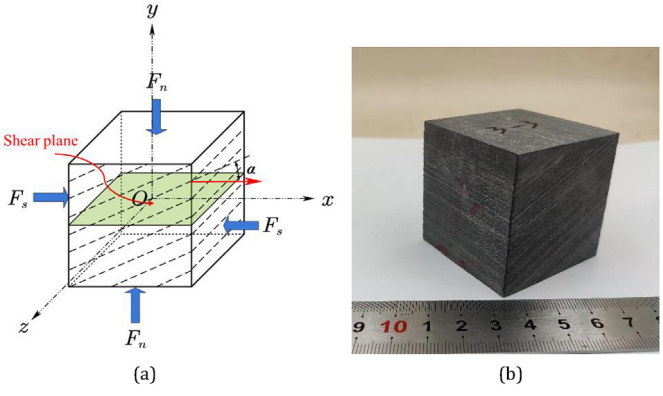

Fig. 1. (a) Schematic of shale sample bedding orientation α and direct shear loading method (F_n is the normal load and F_s is the direct shear load); and (b) Typical 50 mm × 50 mm × 50 mm cubic shale specimen with well-developed bedding.

3. Results and analysis

3.1. Anisotropic properties of shale creep deformation under direct shearing

Fig. 4 shows the trend of multilevel shear-induced creep deformation of the shale specimens with different bedding orientations. All specimens show apparent time-dependent creep deformation above the crack initiation stress under direct shearing path. Regardless of the bedding inclination angle, the creep deformation at each level of shear stress generally goes through two stages: an initial creep stage, in which the shear strain increment per unit time decreases rapidly; and a steady-state creep stage, where the shear creep rate remains essentially constant. Nevertheless, there is a substantial difference in the creep deformation at the same stress ratio level for specimens with different bedding orientations, indicating that shale's anisotropic properties significantly affect time-dependent deformation. Under a higher shear stress, the shale specimens exhibit an acceleration creep stage until failure. Notably, the creep deformation curve in this paper was plotted using all recorded deformation data. The creep deformation increases with elapsed time in an oscillating fashion. However, the

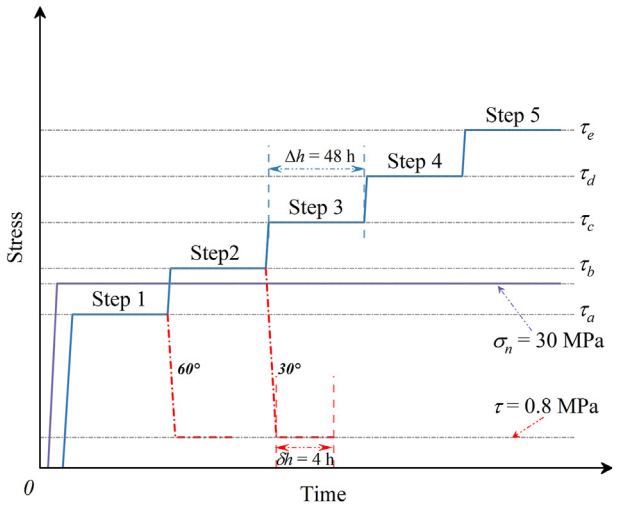

Fig. 3. Schematic diagram of the loading path of the multilevel shear creep and unloading shear creep tests. The solid purple line indicates the normal stress-loading path; the solid blue line indicates the direct shear stress loading path, and the red dashed and dotted lines indicate the unloading path.

Table 1
Shear stress in multilevel shear creep tests of shale specimens with different bedding inclination angles.

Bedding inclination angle, α (°)	τ_a	τ_b	τ_c	τ_d	τ_e
0	22.82	28.09	33.36	38.62	49.15
30	27.22	33.51	39.79	46.07	52.36
45	27.92	34.37	40.81	47.26	53.70
60	28.20	34.70	41.21	47.71	54.22
90	31.76	39.08	46.41	50.37	–

Note: τ_a, τ_b, τ_c, τ_d and τ_e are the first, second, third, fourth and fifth levels of direct creep stress, respectively.

amplitude of fluctuation does not affect the processing of creep data (Geng et al., 2017; Herrmann et al., 2020). Fig. 5 shows the evolution of partially enlarged creep deformation over elapsed time. The creep curve suddenly increases at specific time periods, a phenomenon also known as "pop-ins" (Wang et al., 2020). This is caused by local fracture occurrence in the specimens during the shear creep process (Li et al., 2017).

Rock creep deformation is dependent on the magnitude of stress (Naumenko et al., 2009; Zhao et al., 2018). However, there is a scarcity of literature investigating the stress dependence of direct shear anisotropic deformation behavior for shale. To obtain the elasto-visco-plastic deformation properties of shale under low shear stress conditions (see Figs. 4), Fig. 6 presents the time-dependent deformation properties of shale with five different bedding inclinations. Since each set of deformation data was recorded at a different stress level, the creep compliance of shale with five different bedding orientations was calculated to compare the shear creep deformation response of shale with varying inclinations of bedding under a low shear stress. The results include characteristics of the long-term shear deformation behavior, as shown in Fig. 6a. Under all bedding inclinations, the creep compliance of shale rises approximately linearly with logarithm of time. The creep compliance exhibits anisotropic properties under different bedding inclinations, similar to the elastic properties (Sone and Zoback, 2013a; Geng et al., 2017). To analyze the change in creep compliance with bedding inclination over time, Fig. 6b shows the creep compliance at different creep time scales ($t = 0.5$, 1, 2, 4, and 8 h). Regardless of the bedding orientation, the creep compliance increases with elapsed time, indicating that the damage of shale during deformation is continuously accumulating. The difference in creep compliance change is significant under different bedding inclinations. When the deformation time is 8 h, the creep compliance of the shale specimens with $\alpha = 30°$ is the largest, and the creep compliance of specimens with $\alpha = 60°$, 90°, 0°, and 45° decreases successively. Furthermore, the relative magnitude of shale creep compliance varies with creep time scales and bedding inclination angles. For example, at shorter time scales (e.g. $t = 1$ h), the creep compliance of shale specimens with $\alpha = 60°$ is greater than that of shale specimens with $\alpha = 30°$. However, as the creep time increases, the creep compliance of shale specimens with $\alpha = 30°$ begins to exceed that of shale specimens with $\alpha = 60°$. This gap becomes more prominent with elapsed time. Thus, it is necessary to analyze the evolution of the anisotropic creep compliance of shale at different creep time intervals. As shown in Fig. 6c, during the creep time interval of $t = 0.5$–8 h, the increment of creep compliance of shale specimens at $\alpha = 30°$ is the greatest, and those of the creep compliance of the specimens at $\alpha = 90°$, 0°, 60°, and 45° decrease consecutively. It is noticeable that the increase percentage and increasing rate of the creep compliance at $\alpha = 0°$ exceed those at $\alpha = 30°$ after 4 h of creep. Thus, under engineering time scales (shale gas extraction generally lasts for several years or even decades), the shear creep deformation of shale at $\alpha = 0°$ may be the most significant. In summary, bedding inclination has a substantial control of the direct shear creep behavior of shale, even under low shear stress conditions.

To distinguish the elastic and viscous components from the total strain during the shear loading and unloading stages, this study conducted unloading creep tests on shale with $\alpha = 30°$ and 60°. Fig. 7a plots the shear stress–strain curves during the pure loading and unloading stages (excluding creep). For the unloading stage, the rate of recovery of shear strain exhibits a trend of a gradual increase to a constant value, and the shear modulus g_α during the constant stage of strain recovery rate satisfies $g_{30°} > g_{60°}$. As a result, the recovery shear strain value of shale specimen with $\alpha = 30°$ in the unloading stage is greater than that of $\alpha = 60°$. The instantaneous plastic strains of shale at $\alpha = 30°$ and 60° are 17% and 20% of the peak shear strain during the loading stage, respectively, which also causes the loading–unloading shear stress–strain curve to form a hysteresis loop. Fig. 7b further analyzes the energy dissipation during loading and unloading for these two bedding orientations. The energy dissipation of $\alpha = 30°$ and 60° shale respectively accounts for 36% and 40% of the total strain energy during the loading and unloading stages. This indicates that more energy is used to generate nonelastic strain in the specimen with $\alpha = 60°$ during the shear loading and unloading process. It is impossible to distinguish between viscoelastic and viscoplastic creep due to the lack of creep tests after unloading in most shale creep studies (Chau et al., 2017). Based on the deformation curve when unloading to 0.8 MPa (see Fig. 3), the time-dependent deformation curves in the creep stage and the delayed elastic recovery stage are plotted in Fig. 7c (for comparison, the sign of the delayed recovery strain in Fig. 7c is reversed). The creep and delayed recovery strains of specimens with $\alpha = 30°$ and 60° exhibit a linear relationship with the logarithm of time. As shown in Fig. 7d, within the initial 4 h, the delayed elastic recovery strains of specimens with $\alpha = 30°$ and 60° are 9.4×10^{-4} and 2.5×10^{-4}, respectively, whereas the creep strains of shale during the same time period are 6.5×10^{-4} and 5.2×10^{-4}, respectively. At $\alpha = 30°$, the delayed elastic recovery strain of shale during the initial 4 h is significantly greater than the creep strain, indicating that recoverable deformation is also generated during the process of pure loading of the creep stress. Overall, the shear deformation is primarily of elastic and viscoelastic deformation. At certain bedding orientations (such as 30°), it is challenging to separate viscoelastic

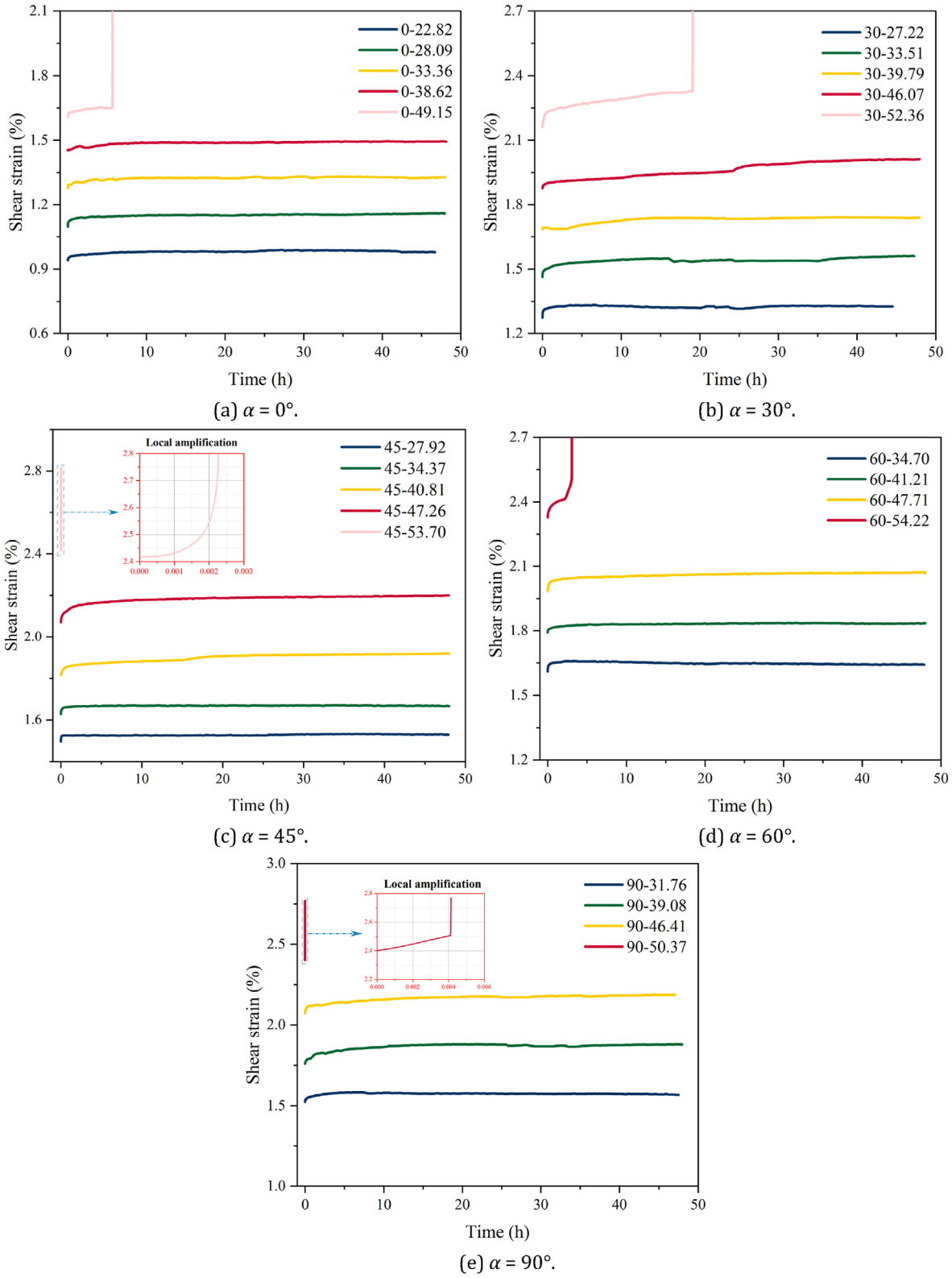

Fig. 4. Creep deformation evolution of shale with different bedding orientations under multiple levels of shear stress. The legend is labeled as number-number; the first number is the bedding inclination angle while the second number is the level of shear creep stress. For example, 60–34.70 means the shear strain of the specimen with bedding inclination angle of 60° under the direct shear stress of 34.70 MPa.

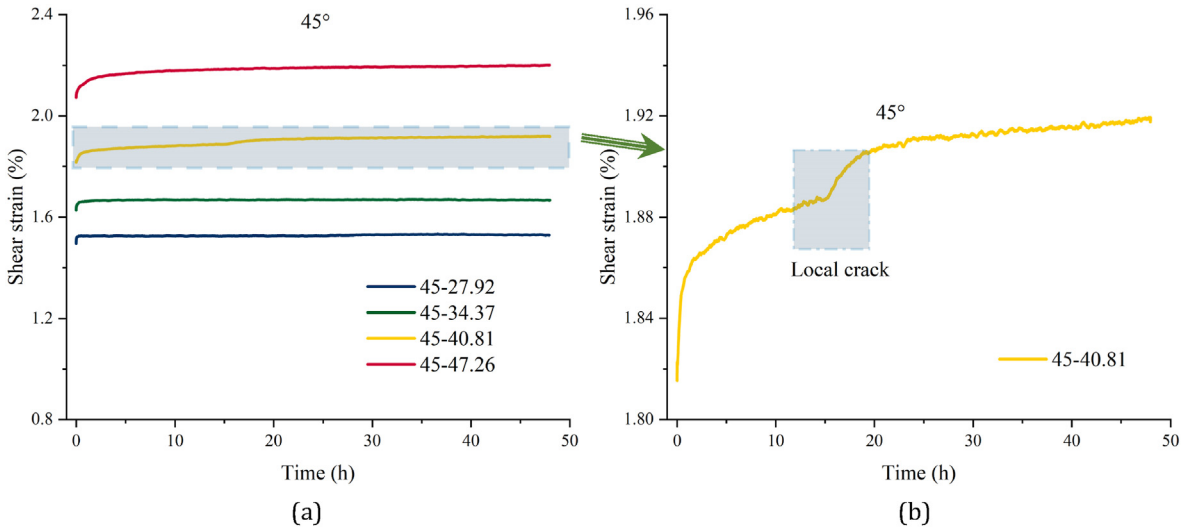

Fig. 5. (a) Shear strain–time deformation curve plotted by all the recorded shear deformation data; and (b) Partial enlarged view of the shear strain–time deformation curve. The legend is the same as that of Fig. 4.

strain and viscoplastic strain merely by unloading creep tests. This may be attributed to the fact that the shear stress applied does not follow a specific stepwise function of time (Hilsdorf and Müller, 1983), or it may be caused by the complex failure mechanisms associated with shale anisotropy, which requires further investigation.

To analyze the creep properties under different shear stress levels, the creep deformation of anisotropic shale specimens under high shear stress conditions is analyzed. Since shale specimens at $\alpha = 45°$ and 90° entered the accelerated creep stage directly after the final level of shear stress was applied, the pre-level creep deformation data of the shale specimens were selected for analysis under these two bedding inclinations. Fig. 8a and b shows the development of the shale specimens' creep compliance in the initial, steady-state, and accelerated stages with different bedding orientations over elapsed time in semilogarithmic and double-logarithmic coordinates, respectively. Compared with those under low shear stress conditions (see Fig. 6), the anisotropic properties of the shale creep compliance under high shear stress conditions are more complex. The values of the shale creep compliance at different creep time scales (such as 0.5, 1, 2, 4, and 8 h) under different bedding orientations are significantly dispersed, making it difficult to qualitatively and quantitatively characterize the control of bedding orientation on the direct shear creep behavior of shale. Further analysis shows that in the coordinates (see Fig. 8a), the slope of the creep compliance variation curve increases gradually in the initial creep stage, then stabilizes at a particular value in the steady-state creep stage, and ultimately rises dramatically in the accelerated creep stages. In contrast, in double-logarithmic coordinates (see Fig. 8b), the rate of increase in the creep compliance in the initial and steady-state creep stages slows, the attenuation rate decreases gradually, and it eventually rises dramatically in the accelerated creep stage till failure. The trends of change in the creep compliance in different coordinate systems present opposite phenomena in the initial and steady-state creep stages, suggesting the complexity of the creep mechanism of shale under shear. Simultaneously, without considering accelerated creep, the creep compliance of the shale specimens with $\alpha = 0°$ remains at the minimum within more than 98% of the creep time, followed by 90°. However, the dispersion of creep compliance at other angles remains high, making it difficult to intuitively identify the relative magnitude of creep compliance at $\alpha = 30°$, 45° and 60° under high shear stress conditions. To further characterize the anisotropic properties of creep deformation under a high shear stress, Fig. 8c presents the evolution of the overall slope of the creep compliance curve (without considering the accelerated creep stage) with respect to the bedding orientation in semilogarithmic and double-logarithmic coordinates, K_1 and K_2, respectively. Both K_1 and K_2 show an increasing trend at first before decreasing with bedding orientation. K_1 reaches its minimum and maximum at $\alpha = 0°$ and 45°, respectively, while K_2 reaches its minimum and maximum at $\alpha = 90°$ and 60°, respectively. This is because, compared with K_1, K_2 in double-logarithmic coordinates places more emphasis on describing short-term strain (Bažant and Chern, 1983), which results in a large curvature in the creep compliance curve of shale with some bedding orientations in double-logarithmic coordinates, i.e. using a larger K_2 value to fit short-term creep compliance data. However, the primary objective of conducting rock creep studies is to predict the long-term mechanical properties of rock. Therefore, we need to discuss the practical application of K_1 and K_2. If K_1 is an effective metric, shale with $\alpha = 0°$ would have the minimum creep compliance under direct shearing, with the creep compliance increasing successively in the order of $\alpha = 90°$, 30°, 60°, and 45°. If K_2 is an effective metric, it yields that shale with $\alpha = 90°$ would have the minimum creep compliance, which rises successively at $\alpha = 0°$, 30°, 45°, and 60°. Compared with the test data, it is apparent that K_1 provides more consistent predictions than K_2. This suggests that for the quantitative characterization of shale anisotropic creep behavior under direct shearing, a logarithmic model is acceptable (superior to the power law model). This will be discussed in Section 4.1.

The determination of the inception of accelerated creep has a significant impact on engineering practice, such as wellbore instability. The starting point of accelerated creep can determine the threshold of the mechanical parameter evolution of shale. Fig. 9 shows the stress τ_e and strain γ_t corresponding to the shear-induced accelerated creep onset in anisotropic shale samples. As the bedding orientation increases, both τ_e and γ_t show an increasing trend followed by a decreasing trend. Both τ_e and γ_t reached their minimum values at $\alpha = 0°$ and maximum values at $\alpha = 60°$. This indicates that time-dependent fractures along bedding planes can be easily activated when the bedding plane is parallel to the shear loading. Shear accelerated creep is most difficult to occur at an angle of $\alpha = 60°$ because the maximum

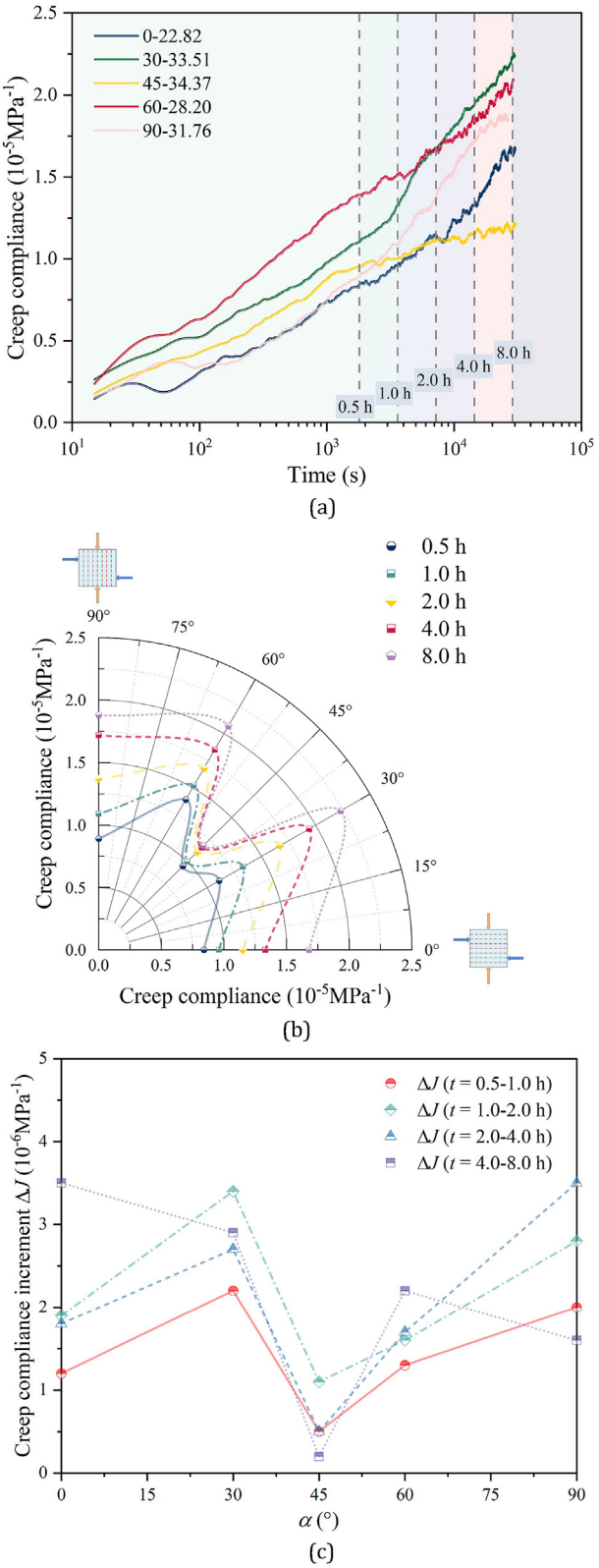

Fig. 6. (a) Creep compliance evolution of shale with five bedding orientations under a low shear stress (the legend is the same as that of Fig. 4); (b) Creep compliance of shale with five bedding orientations under different creep time scales (t = 0.5, 1, 2, 4, and 8 h) and a low shear stress; and (c) Creep compliance increment of shale with five bedding orientations in different time periods ΔJ under a low shear stress.

deformation is required to activate time-dependent fractures at this bedding orientation. For comparison, the normalization method is used to describe the variation trend of ξ (the ratio of τ_e to γ_t) with respect to bedding orientations. In the normalization process, ξ was set to 1 at $\alpha = 0°$, based on which ξ at other bedding orientations is calculated (see Fig. 9). The results show that ξ value decreases with increasing bedding orientation α. When α changes from 0° to 30°, the ξ value decreases rapidly; the ξ value at $\alpha = 30°$ is 75% of that at $\alpha = 0°$. When α increases from 30° to 90°, the ξ value decreases linearly at a constant rate with increasing bedding orientation, i.e. ξ can be considered a monotonically decreasing function of bedding orientation α. This indicates that the data processing method in this study can effectively simplify the construction of functions to represent anisotropic creep. Moreover, the minimum ξ value of the shale specimens is approximately 70% of the maximum value, providing a critical boundary condition for quantitatively evaluating the anisotropic function of creep failure.

3.2. Anisotropy of shale steady-state creep rate under direct shearing

The test results indicate that the steady-state creep stage dominates the longest time in the entire creep process. Since shale gas production typically lasts for several years or even decades, it is imperative to further investigate the anisotropic steady-state creep behavior of shale samples. Fig. 10 shows the shale steady-state creep rate variation trend with bedding orientations and shear stress plotted on semilogarithmic coordinates. As shown in Fig. 10a, the steady-state creep rate of shale rises with increasing shear stress, irrespective of the bedding orientation. Under low shear stress levels ($\tau \leq 41$ MPa), the steady-state creep rate of shale at $\alpha = 0°$ is approximately ten times higher than that at other bedding orientations. Under high shear stress levels ($\tau > 41$ MPa), the steady-state creep rate of shale at $\alpha = 30°$, 45°, 60°, and 90° increases significantly with bedding orientation, and the difference with the steady-state creep rate of shale at $\alpha = 0°$ decreases to within one order of magnitude. This indicates that anisotropy and shear stress significantly affect the shale steady-state creep rate. Based on previous studies (e.g. Bažant and Chern, 1984; Brantut et al., 2014), the power law function and the exponential function are used to quantitatively analyze the relationship between the anisotropic steady-state creep rate of shale and shear stress:

$$\dot{\gamma}_{ste} = a\tau^b \tag{1}$$

$$\dot{\gamma}_{ste} = h\exp(u\tau) \tag{2}$$

where $\dot{\gamma}_{ste}$ is the steady-state creep rate; a, b are the fitting parameters of the power law function; and h, u are the fitting parameters of the exponential function.

Fig. 10b and c shows the fitting results of Eqs. (1) and (2), respectively. The fitting coefficient R^2 for both functions is greater than 0.8 in most cases, indicating that both functions can adequately describe the trends of steady-state creep rate with changing shear stress and bedding orientation. Notably, in semilogarithmic coordinates, when the shear stress is high, the power law function (see Eq. (1)) tends to underestimate the steady-state creep rate, while the exponential function (see Eq. (2)) has a better fitting effect. Conversely, at a lower shear stress, the exponential function significantly underestimates the steady-state creep rate, whereas the power law function more accurately describes the development of the steady-state creep rate. The

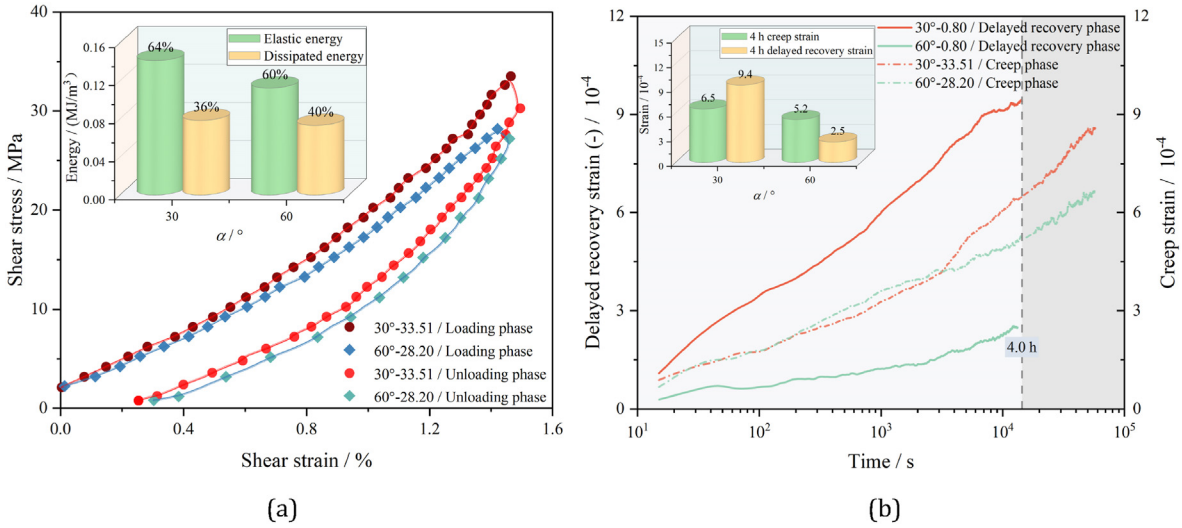

Fig. 7. (a) Comparison of the instantaneous deformation of shale with bedding orientations of 30° and 60° during low shear loading and unloading stages; and (b) development of the creep deformation of shale with bedding orientations of 30° and 60° during the creep deformation stage and delayed elastic recovery stages.

analysis shows that the power law function and exponential function can characterize the relationship between the steady-state creep rate and shear stress within only a specific stress range. Unfortunately, both cannot reflect the stress dependence of the steady-state creep rate during the hardening and damage process of shale (Sone and Zoback, 2013a). This is because some studies (e.g. Bažant and Chern, 1983) uniformly plot the original data obtained from shale creep tests and the calculated values of the theoretical model in logarithmic space, which largely disregards the deviation of the calculated values from the experimental data. To predict the variation in the shale steady-state creep rate under any shear stress, a semilogarithmic model is proposes in the study that can characterize the evolution of the steady-state creep rate with shear stress, based on the linear relationship between the logarithm of the steady-state creep rate and shear stress:

$$\log_{10}\dot{\gamma}_{ste} = c + d\tau \tag{3}$$

where c and d are the fitting parameters of the semilogarithmic model.

In Eq. (3), the intercept c represents the logarithmic form of the steady-state creep rate of the shale specimens when the shear stress approaches 0. Despite the challenge of directly testing c with current experimental testing techniques, this approach indicates that the initial creep stage will inevitably evolve into the steady-state creep stage under a particular shear stress, regardless of the variations of the bedding orientations and shear stress. This is because new stress concentration points are inevitably generated during creep deformation, continuously activating new creep (Chau et al., 2017). The slope d reflects the stress dependence of the steady-state creep rate of shale at different bedding orientations. The larger the slope d, the higher the stress dependence of the steady-state creep rate of shale. Additionally, it is noted that in a semilogarithmic coordinate system, when the shear stress approaches the failure stress, the slope of the steady-state creep rate–stress curve at $\alpha = 0°$ is the greatest (see Fig. 10a). Thus, taking steady-state creep rate data at $\alpha = 0°$ as an example, Fig. 10d compares the newly proposed semilogarithmic model (Eq. (3)), the power law function, and the exponential function with experimental data. Compared with the power law and exponential function, the semilogarithmic model can better characterize the steady-state creep rate evolution under shear stress, reducing the deviation of the calculated results from the experimental steady-state creep rate data.

To better unserstand the capacity of the semilogarithmic model (Eq. (3)) to represent the anisotropic steady-state creep rate of shale under different shear stresses, Fig. 11a shows the representation of the semilogarithmic model for the steady-state creep rate evolution of shale specimens with five different bedding orientations. It seems that the trend of the steady-state creep rate of shale, with various bedding orientations, can be characterized by the semilogarithmic model at the changing shear stress. However, the slope and intercept of the fitting curve show significant differences. Fig. 11b further shows the evolution of the semilogarithmic model parameters c and d with bedding orientation α. As α increases, the intercept c of the semilogarithmic model shows a downward trend before rising. The value of c is the greatest when $\alpha = 0°$ and is the least when $\alpha = 60°$. This indicates that shale is most prone to shear creep deformation at $\alpha = 0°$, while $\alpha = 60°$ is the bedding orientation where it is most difficult for shale to undergo creep deformation. The slope of the semilogarithmic model, d, increases initially and then decreases with increasing α. The value of d peaks when $\alpha = 60°$, at approximately twice its minimum value ($\alpha = 0°$). This is because the propagation of shear sliding through the bedding and matrix is more complex than that of simple shear sliding along the bedding. Simultaneously, the intercept of the semilogarithmic model, c, and the slope, d, are not monotonic functions of the bedding orientation α. This is because the tensile action induced by direct shear stress further promotes shear sliding along the bedding with increasing shear stress, reducing to some extent the energy required for shear penetration through the bedding and matrix along the predetermined shear plane. In addition, the bedding orientation significantly affects the energy distribution applied to the specimen, resulting in a significant anisotropy in the steady-state creep rate of shale. The above analysis shows that the newly proposed semilogarithmic model can effectively characterize the shale steady-state creep rate at different bedding inclinations and shear stress levels.

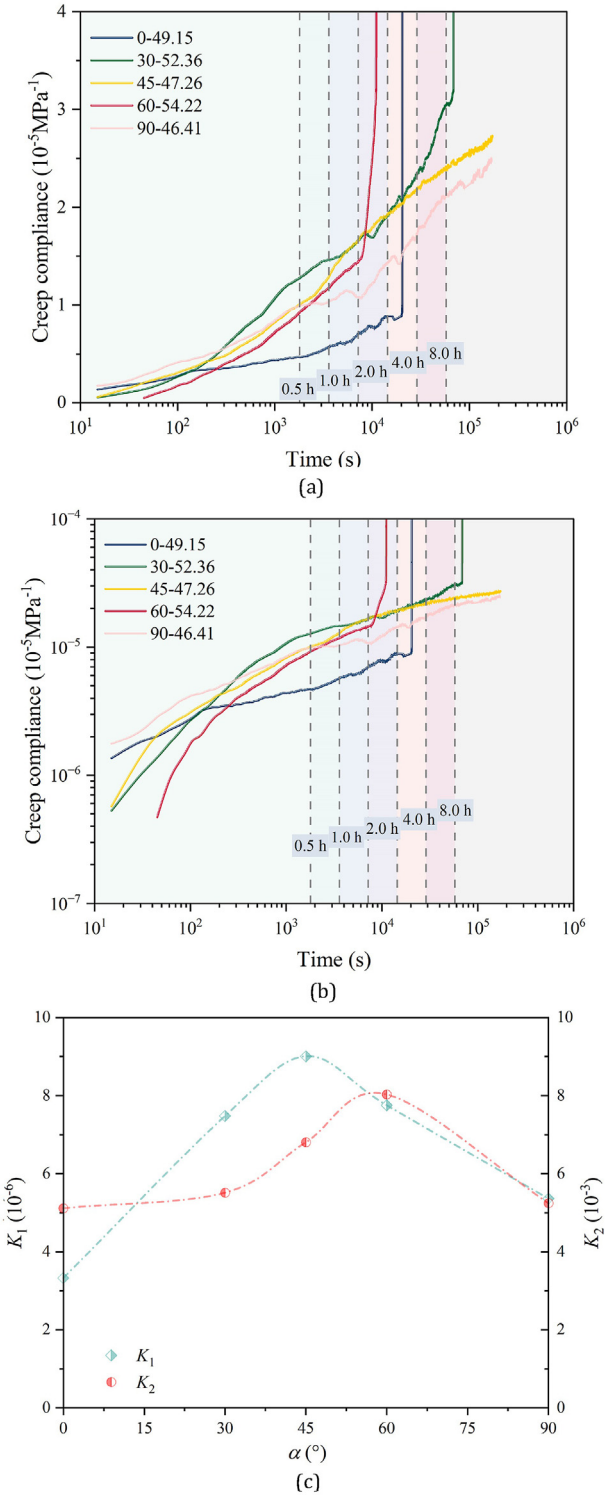

Fig. 8. (a) Evolution of anisotropic creep compliance of shale with five bedding orientations in semilogarithmic space under a high shear stress; (b) Evolution of anisotropic creep compliance of shale with five bedding orientations in double-logarithmic space under a high shear stress; and (c) Evolution of the overall slopes K_1 and K_2 of the creep compliance curves (without considering the accelerated creep stage) with different bedding orientations in semilogarithmic and double-logarithmic coordinates.

4. Discussion

4.1. Applicability of empirical creep models for representing shear creep behavior

Empirical creep models have been extensively studied due to the simplicity, ease of understanding and application. While empirical creep models can adequately fit experimental data, the ability to predict long-term creep deformation is questionable. Moreover, it is difficult to determine the superiority of different empirical models in some cases. For shale, there is also controversy over the consideration of shale's intrinsic anisotropic properties by empirical models. Consequently, it is necessary to evaluate the empirical creep models in representing shale's anisotropic creep behavior under direct shear. Currently, the commonly used equations for empirical creep models include the following equations (Bažant and Chern, 1983, 1984; De Schutter, 1999; Brantut et al., 2013; Sone and Zoback, 2014):

(1) Power law model

$$\gamma = A_0 t^m \tag{4}$$

(2) Logarithmic model

$$\gamma = A_1 + B_1 \log_{10} t \tag{5}$$

(3) Exponential model

$$\gamma = A_2\left(1 - B_2 e^{-t/t_0}\right) \tag{6}$$

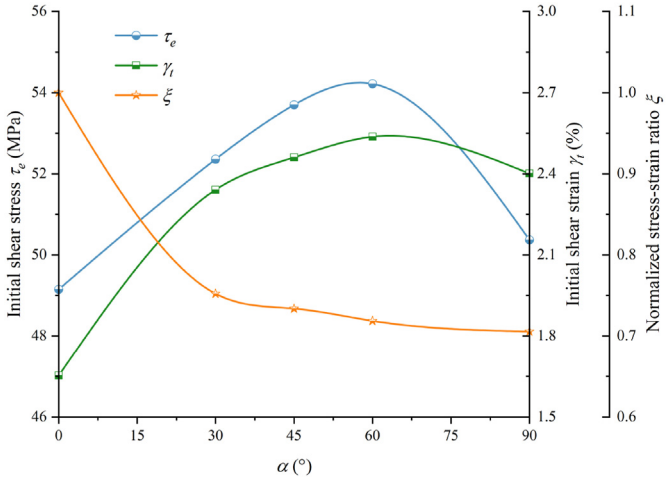

Fig. 9. The shear stress τ_e, strain γ_t, and the corresponding normalized stress–strain ratio ξ of shale specimens with different bedding orientations upon accelerated creep.

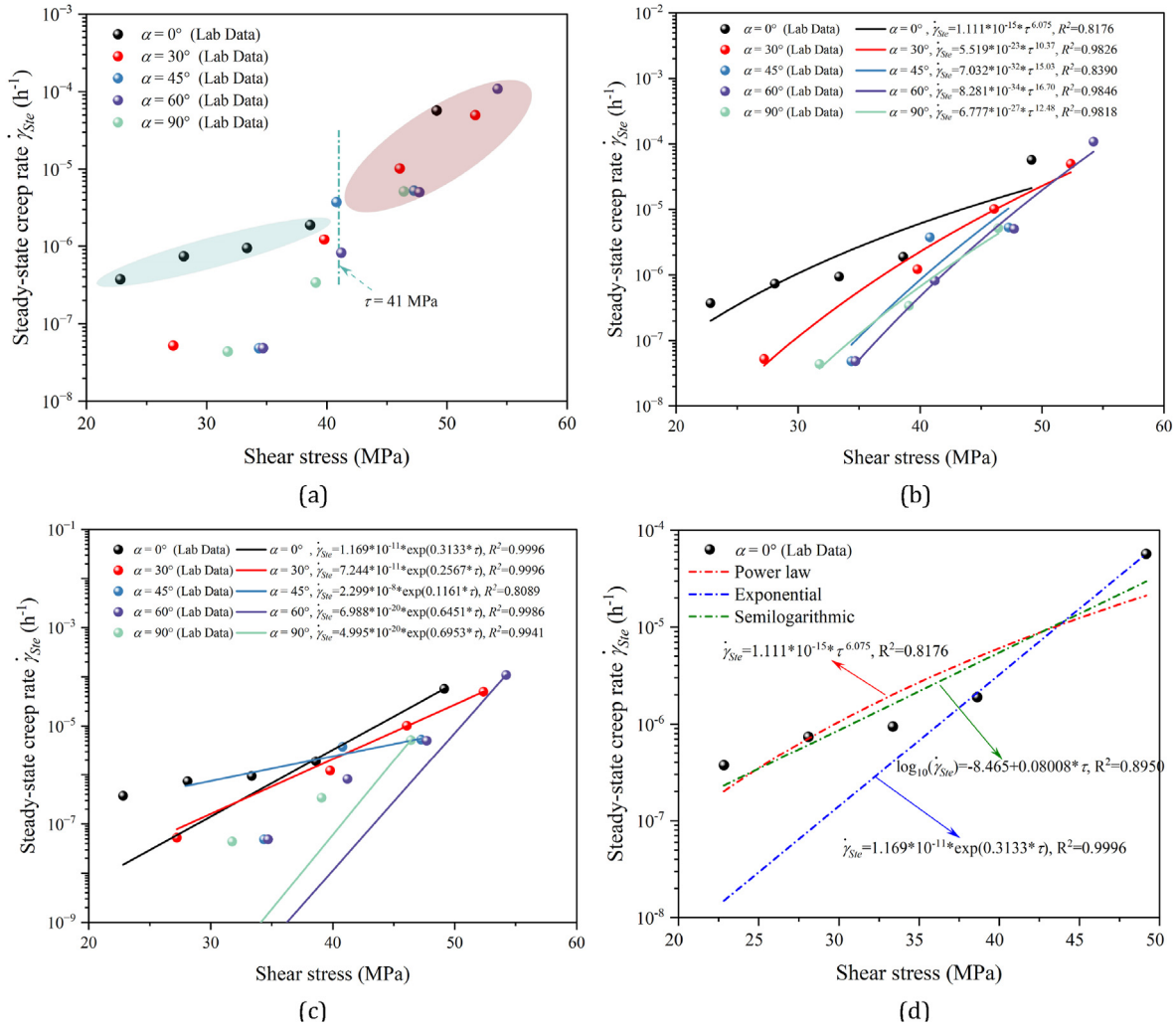

Fig. 10. (a) Variation in shale steady-state creep rate with shear stress in semilogarithmic space at different bedding orientations; (b) Power law function fitting of the shale steady-state creep rate under different shear stress levels and bedding orientations; (c) Exponential function fitting of the shale steady-state creep rate under different shear stress levels and bedding orientations; and (d) Comparison of the shale steady-state creep rate fitting capacity of the semilogarithmic model, power law function, and exponential function (taking the steady-state creep rate data of shale at $\alpha = 0°$ as an example).

(4) Hyperbolic model:

$$\gamma = \frac{t}{A_3 + B_3 t} \tag{7}$$

(5) Crack damage creep model (Zhao et al., 2017)

$$\gamma = A_4 e^{-B_4/\ln(kt)} \tag{8}$$

where γ represents the creep strain; t is the creep time; and A_i (i = 0, 1, 2, 3, 4), B_i (i = 1, 2, 3, 4), m, t_0, and k are the fitting parameters.

Notably, most researchers have verified empirical creep models merely from the perspective of creep deformation. However, compared with creep deformation, the creep rate is more sensitive to experimental conditions (Liu et al., 2021a). The evolution of the creep rate is equally important from a physical mechanism perspective, and its study facilitates the connection between the macroscopic creep behavior of rocks and the microscopic mechanisms (Ishibashi et al., 2016). Thus, it is also crucial to study the rationality of the empirical creep models by analyzing the evolution of the creep rate throughout the entire direct shear creep process. The corresponding formulas for calculating the creep rate for the five empirical creep models mentioned above are as follows:

$$\dot{\gamma} = A_0 m t^{m-1} \tag{9}$$

$$\dot{\gamma} = \frac{B_1}{t \ln 10} \tag{10}$$

$$\dot{\gamma} = A_2 B_2 e^{-t/t_0} \Big/ t_0 \tag{11}$$

$$\dot{\gamma} = \frac{A_3}{(A_3 + B_3 t)^2} \tag{12}$$

$$\dot{\gamma} = \frac{A_4 B_4 e^{-B_4/\ln(kt)}}{[\ln(kt)]^2 t} \tag{13}$$

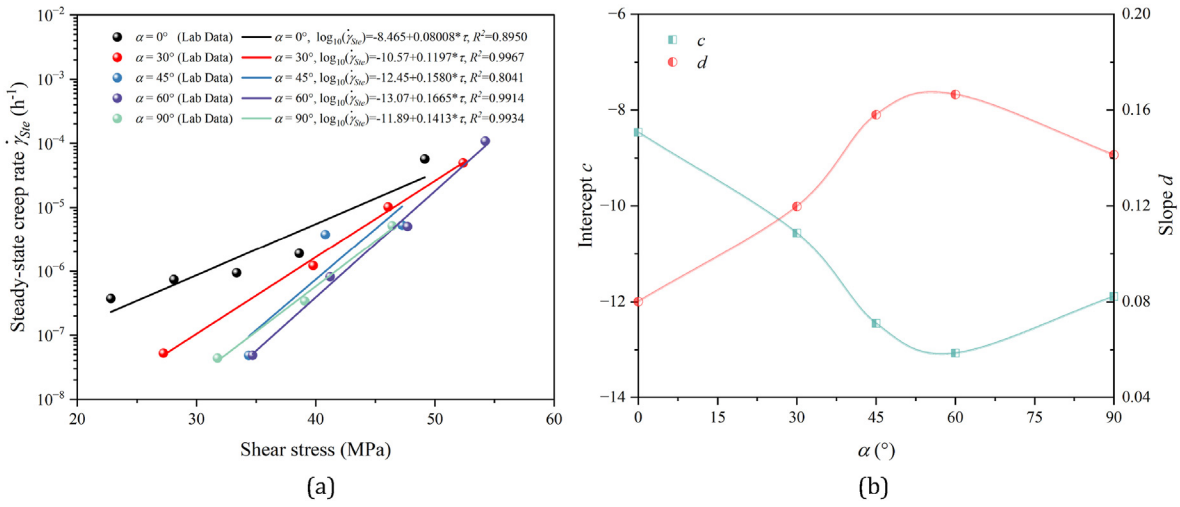

Fig. 11. (a) Representation of the steady-state creep rate evolution of shale specimens with five bedding orientations by the semilogarithmic model, and (b) Variations in the intercept c and slope d of the semilogarithmic model with bedding orientation α.

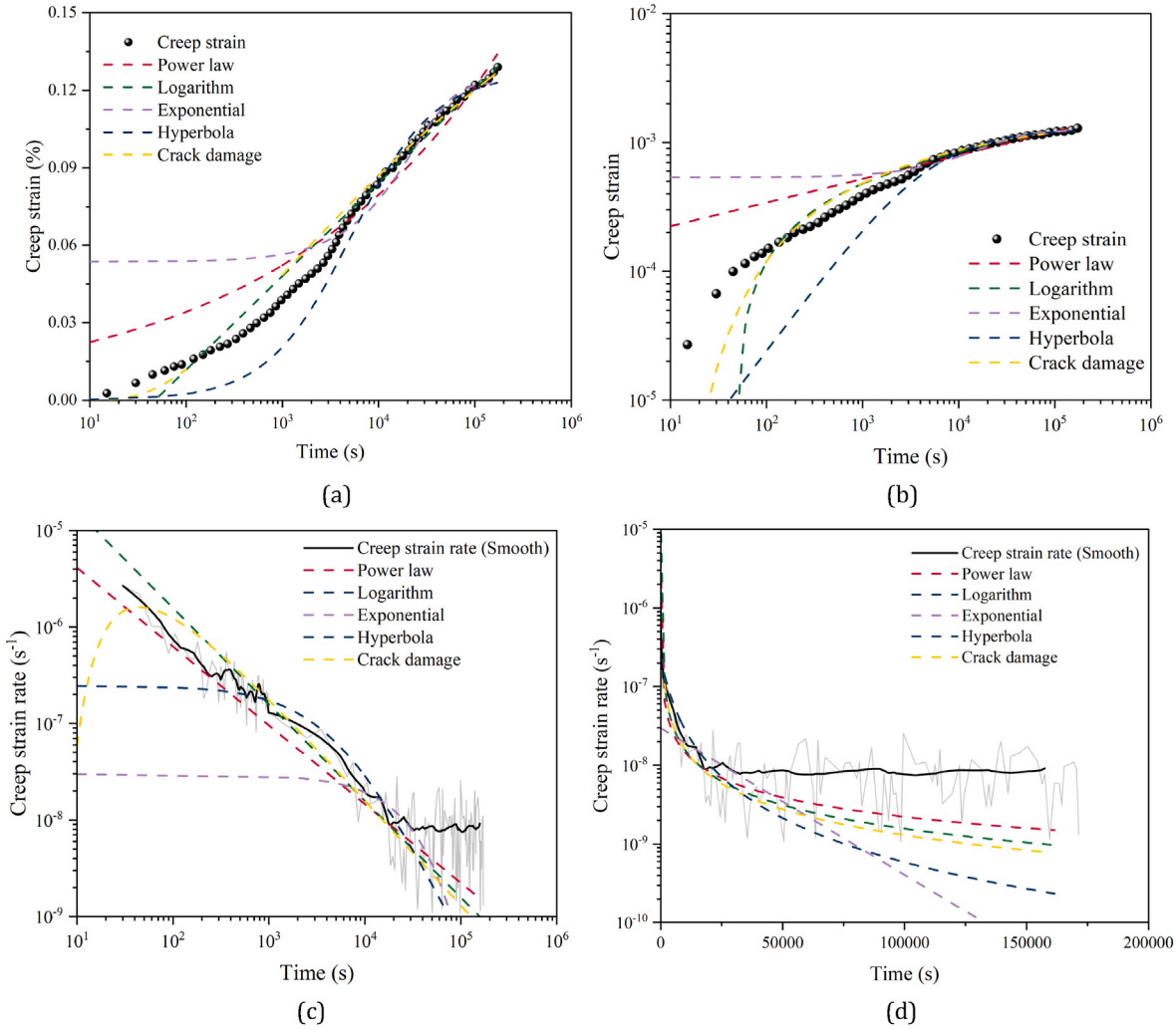

Fig. 12. (a) Evolution of creep strain with time fitted by five empirical creep models in semilogarithmic space; (b) Evolution of creep strain with time fitted by five empirical creep models in double-logarithmic space; (c) Comparison of the creep rate calculated by the five empirical creep models with the experimental values in logarithmic space; and (d) Comparison of the creep rate calculated by the five empirical creep models with the experimental values in semilogarithmic space, taking direct shear creep data of shale specimen 45–47.26 as an example. It is noted that (c) and (d) show smooth creep rate curves because all the recorded deformation–time data that are used to derive the creep rate yield noisy results; for comparison, the complete fluctuating creep rate data are shown with the light gray lines.

Fig. 12 shows the creep and creep rate fitting curves obtained using different empirical creep models (using the shale creep test data under $\alpha = 45^\circ$ and $\tau = 47.26$ MPa as examples; creep time of 48 h). The corresponding fitting parameters and fitting correlation coefficients R^2 are given in Table 2. Fig. 12a and b shows that all the tested empirical creep models can accurately fit the creep strain data after a creep time of $t \geq 5000$ s. In particular, the fitting coefficient R^2 of the crack damage creep model is as high as 0.9862 at 48-h testing time, and the power law model with the lowest fitting coefficient still returns an R^2 value as high as 0.8848. This indicates that it is difficult to directly evaluate the advantages and disadvantages of the five empirical creep models based on the creep strain–time curves. The evolution curves of the creep rate corresponding to the five empirical creep models are obtained (see Fig. 12c and d) by substituting the parameters obtained from the creep strain fit into Eqs. 9–13. From Eqs. (9) and (10), we know that in double-logarithmic space, the slope of the creep rate predicted by the power law model is m-1, and the slope of the creep rate predicted by the logarithmic model is $-\log_{10}(\ln(10))$. Fig. 12c shows that these two types of models seem to fit the experimental data well; but in semilogarithmic space (Fig. 12d), these models still deviate from the test data. However, these two models are closer to the test data than the other empirical models. In addition, the curve of the logarithm of the exponential model-predicted creep rate with time is a straight line with a constant slope of $-\log_{10}(e/t_0)$, but the constant slope obviously disagrees with the experimental results (see Fig. 12c and d). Notably, the exponential model assumes that the mechanical behavior is independent of the deformation history, which is inconsistent with the fact that the creep behavior of shale depends on the deformation history and stress path (Palmer et al., 2007). The hyperbolic model predicts that the square of the creep rate is inversely proportional to time and that its characterized creep rate decays with time at an accelerating rate far greater than those of the power law and logarithmic models. This ultimately leads to the creep deformation approaching its final value in a short period of time, which is apparently inconsistent with the creep rate change pattern shown in Fig. 12c and d. At the same time scale, no evidence of creep deformation termination has been found in existing creep experiments of exceptionally long durations. This is because there will always be a location of stress concentration that causes the propagation and creep of microcracks under constant stress (Chau et al., 2017; Kong et al., 2023). The crack damage creep model predicts that the creep rate will rapidly increase to a maximum value in a short period of time, followed by a dramatic decrease, which contradicts the experimental trends shown in Fig. 12c and d. In summary, all five commonly used empirical creep models can approximate the evolution of the creep strain with elapsed time. However, only the power law and logarithmic models can predict the creep rate effectively.

Notably, the above analysis is limited to the fitting ability of empirical models to creep deformation. It is also necessary to evaluate the capability of these empirical models to predict the long-term shear creep behavior of shale, which is more critical for engineering practice and application. In this study, the parameters of the five empirical creep models were fitted using the initial 4-h creep test data. Using specimen 45°-47.26 as an example, Table 2 tabulates the corresponding fitting parameters and correlation coefficient R^2. Then, the same parameters are used to predict the creep behavior from 4 h to 48 h, as shown in Fig. 13. Fig. 12 shows that the creep strain of shale at $\alpha = 45^\circ$ measured at 48 h under $\tau = 47.26$ MPa is 0.129%, which is used as the benchmark for predicting the 48-h shear creep deformation by the five empirical models. It shows that long-term direct shear creep predicted by the power law model significantly overestimates the time-dependent deformation, while the exponential model and the crack damage model predicted values are considerably lower than the benchmark value. This is because when using Eqs. (6) and (7) to predict direct shear creep deformation, the direct creep rate calculated by these two formulas approaches 0 at creep time $t \geq 24$ h (several orders of magnitude smaller than the power law and the logarithmic models), leading to a minimal increase in the subsequent creep strain. The 48-h creep deformation (0.123%) calculated using the hyperbolic model is slightly lower than the benchmark value. As a bounded formula, the hyperbolic model calculates a "final creep value"; however, the creep is likely to continue indefinitely (Brantut et al., 2013). The logarithmic model calculated a prediction value slightly higher than the benchmark value (0.136%); this is because the initial short-term (e.g. 4 h) accumulated strain is not purely "creep behavior", but is influenced by the instantaneous loading stages, which increases the initial slope of the creep strain–time curve. Some scholars (e.g. Geng et al., 2017) simply discard the

Table 2
Five empirical creep model parameters and their correlation coefficients R^2 based on 4-h and 48-h creep data fitting (taking the direct shear creep data of shale specimen 45–47.26 as an example).

Empirical creep model	Parameter for time interval	14,400 s (≈4 h)	172,800 s (≈48 h)
Power law model	A_0	3.076×10^{-5}	1.468×10^{-4}
	M	0.362	0.1836
	R^2	0.9754	0.8848
Logarithmic model	A_1	-8.612×10^{-4}	-6.086×10^{-4}
	B_1	4.248×10^{-4}	3.628×10^{-4}
	R^2	0.9662	0.9834
Exponential model	A_2	9.192×10^{-4}	1.228×10^{-3}
	B_2	0.7843	0.5643
	t_0	4078	23318
	R^2	0.9917	0.9376
Hyperbola model	A_3	2,063,662	4,073,172
	B_3	972.5	789.9
	R^2	0.9755	0.9485
Crack damage creep model	A_4	1.626×10^{-3}	3.643×10^{-3}
	B_4	5.248	11.35
	K	0.1402	0.2776
	R^2	0.7557	0.9862

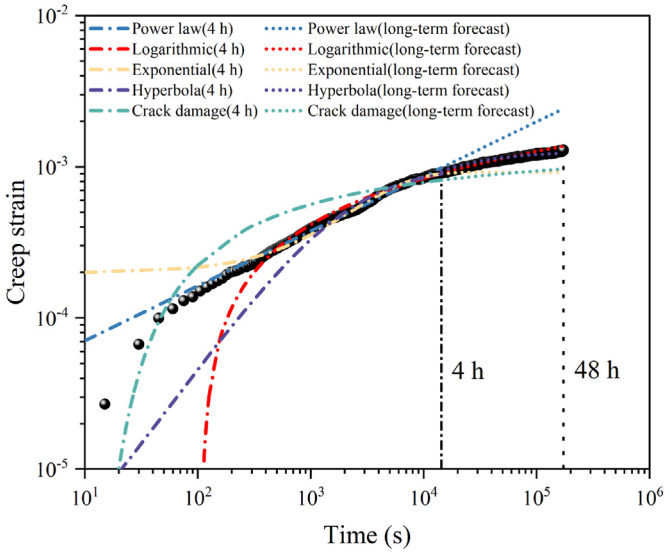

Fig. 13. Five empirical creep model parameters obtained using the initial 4-h test data to predict shear creep deformation results (taking specimen 45–47.26 as an example).

initial short-term accumulated creep strain as instantaneous strain. However, the initial short-term strain contains a significant amount of creep strain, and directly excluding this short-term strain from the logarithmic model significantly reduces the applicability of the model. It suggests that the self-similar characteristics of the logarithmic model can be used to address this deficiency. As the test time increases, the logarithmic model can more accurately rectify the slope of the creep strain–time curve. Due to the limitations of the test conditions, a creep test over an infinite period of time is impractical. For this, it is necessary to analyze the time of the creep test needed to fit the logarithmic model parameters.

Fig. 14 shows the difference between the predictions of the logarithmic model and the test data. The fitting of the parameters of the logarithmic model is obtained with the experimental data under different time scales (t = 8 h, 16 h, 24 h, 32 h, 40 h, and 48 h). Fig. 14 shows that the longer creep test data are used to fit the model parameters. The predicted creep deformation value of the logarithmic model is closer to the real experimental value. Fig. 15 shows the fitting parameters calculated by the logarithmic model using different time scale test data, fitting correlation coefficient, and margin of error between the predicted value and test value at t = 48 h. Fig. 15a shows that the intercept A_1 of the logarithmic fitting function increases with increasing time; slope B_1 decreases continuously with increasing time scale, but the rate of decay shows a changing pattern of first increasing and then decreasing with increasing time scale. When the creep time t > 44 h, the decay rate of slope B_1 over time is below 1%. Rassouli and Zoback (2018) considered that a 24-h creep test is sufficient to characterize the real creep compliance of shale through short-term (4 h) and long-term (4 weeks) creep tests. It can also be seen from Fig. 14 that when the creep time t > 24 h, the prediction curve of the logarithmic model begins to coincide highly with the test data. In addition, as shown in Fig. 15b, the logarithmic model has an excellent fitting effect for the experimental data under different time scales, and the fitting correlation coefficient R^2 is larger than 0.96. The margin of error between a predicted value of the fitting function and the corresponding experimental data is reduced from 5.7% at t = 4 h to 0.5% at t = 48 h. Evidently, the continuous creep test time of 48 h meets the prediction accuracy of the logarithmic model. In other words, compared with the power law model, exponential model, hyperbolic model and crack damage creep model, the logarithmic model can better explain the creep strain and creep rate measured by the test and can more accurately predict long-term shear creep deformation.

It shows that examining shale's direct shear creep behavior solely in specific relational diagrams may be misleading and raise inevitable doubts. For example, in the creep strain–time graph in log-logarithmic coordinates, extrapolation over a long period of time will obscure larger errors in creep deformation (points farther from the origin in Fig. 13, where smaller changes in the vertical coordinate represent significant changes in strain). To avoid the potential illusion of good consistency between the fitted (or predicted) values of the creep model and experimental data, this paper endeavors to compare the predicted values of creep with experimental data in as many coordinate systems as possible to ensure the rationality and applicability of the selected creep model.

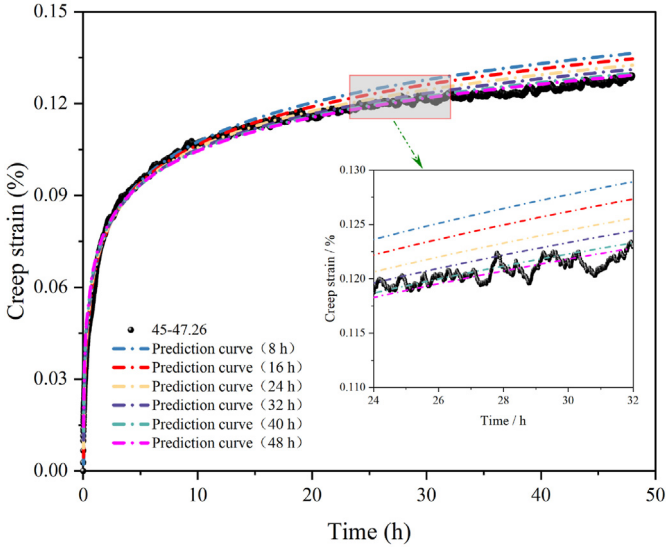

Fig. 14. The logarithmic model parameters calculated based on test data collected at different time scales to predict shear creep deformation results (taking specimen 45–47.26 as an example).

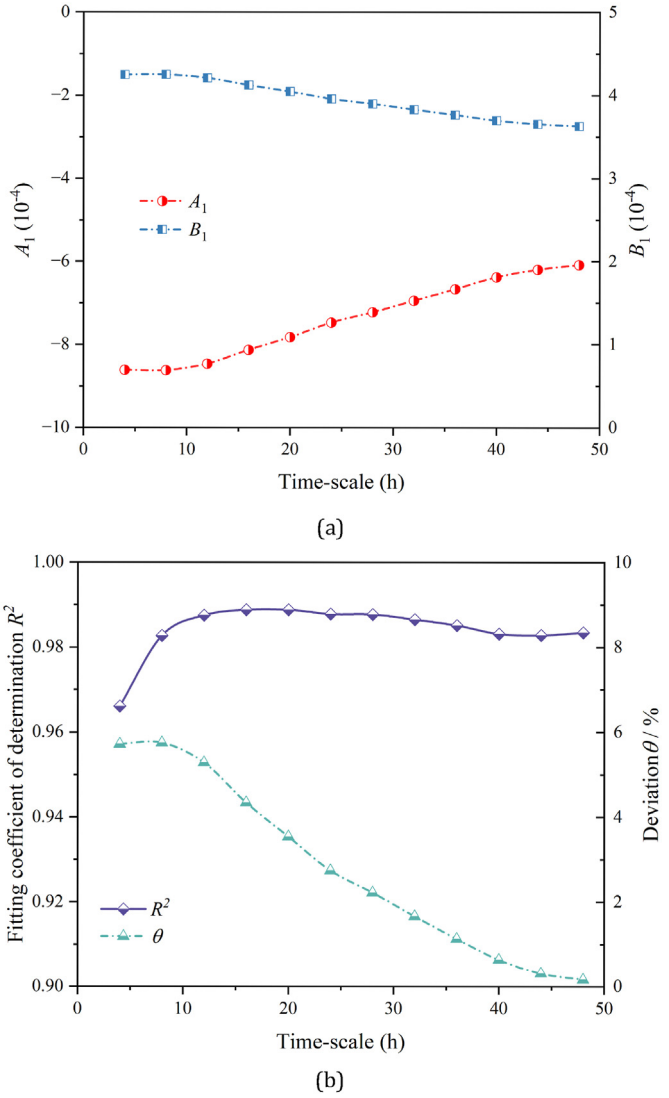

Fig. 15. (a) Evolution of the logarithmic model parameters based on fitting test data collected at different time scales; and (b) Correlation coefficient of the logarithmic model fitted to test data collected at different time scales and the margin of error between the predicted value of the logarithmic model at t = 48 h and the experimental value (taking specimen 45°-47.26 as an example).

4.2. A new mathematical method

In Section 4.1, it indicates that the anisotropic creep behavior of shale under direct shear can be described by the logarithmic empirical model (see Eq. (5)). However, one limitation of Eq. (5) is that it predicts an infinite creep rate at $t = 0$. To eliminate this defect, the logarithmic empirical model can be modified to:

$$\gamma = \delta + \nu \log_{10}(t+1) \tag{14}$$

where δ and ν are the fitting parameters for the modified logarithmic model.

By fitting the creep test data of shale with five different bedding orientations under different shear stresses using Eq. (14), Fig. 16a and b shows the variations in the parameters δ and ν, respectively. The parameters δ and ν exhibit significant scattering, making it challenging to determine the relationship between the fitting parameters and bedding orientation or shear stress. In fact, due to the variation in the shale specimens, some specimens may have more initial microcracks, which may not be fully consolidated under the first level of shear stress (low shear stress). This could result in smaller δ and larger ν values; while under a high shear stress, some specimens may form significant local fractures from microcracks (see Fig. 5), resulting in larger δ and smaller ν values. Under these special circumstances, the discussion of shear creep behavior of shale must consider its internal crack geometry and corresponding mechanical properties. If the data points under these particular circumstances in Fig. 16a and b are not considered, the fitting parameters δ and ν approximate a linear relationship with shear stress, as shown in Fig. 16c and d. The relationships between the parameters δ and ν and shear stress can be represented by the following linear equations:

$$\delta = \lambda_1 + \lambda_2 \tau \tag{15}$$

$$\nu = \mu_1 + \mu_2 \tau \tag{16}$$

where λ_1, λ_2, μ_1 and μ_2 are the fitting parameters.

The fitted correlation equations of Eqs. (15) and (16) are shown in Fig. 16c and d. Although it shows that the dependence of creep on stress is nonlinear, this nonlinearity inevitably complicates the construction of an anisotropic creep model for shale. However, Eqs. (15) and (16) and Fig. 16c and d shows that both the fitting parameters δ and ν have some linear dependence on the shear stress. Thus, it assumes that the nonlinear problem of shear creep stress dependence can be transformed into a linear problem by Eqs. (15) and (16), which significantly reduces the difficulty of quantitatively characterizing the anisotropy of shale shear creep deformation.

To analyze the ability of Eqs. (15) and (16) to consider the anisotropic intrinsic properties of shale, Fig. 17 shows the

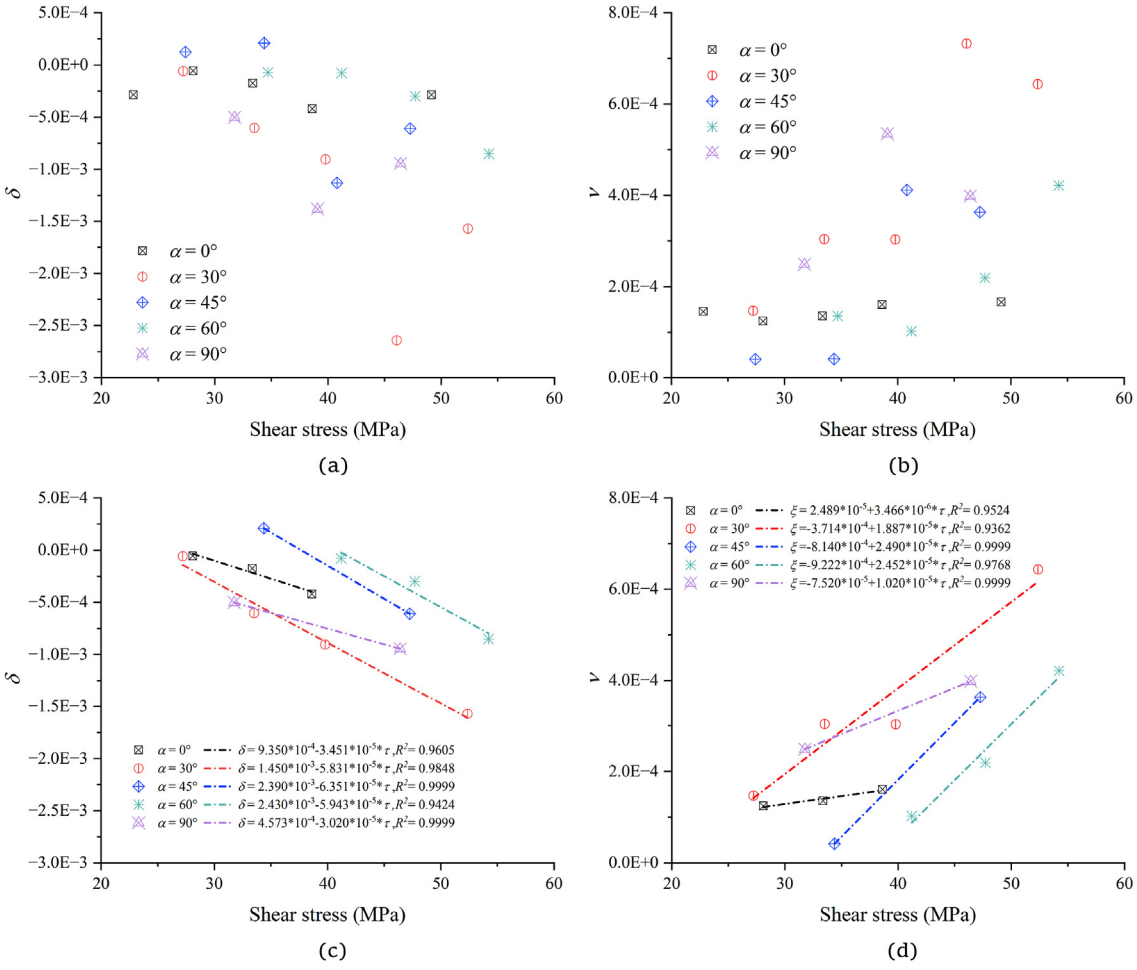

Fig. 16. (a) Variation in parameter δ under different bedding orientations and shear stresses; (b) variation in parameter ν under different bedding orientations and shear stresses; and (c) and (d) the linear fitting equations of parameters δ and ν and the fitting correlation coefficient R^2, respectively.

variations in the parameters λ_1, λ_2, μ_1 and μ_2 with bedding orientation. As the bedding orientation changes from 0° to 90°, λ_1 and μ_2 show a trend of first increasing and then decreasing, while λ_2 and μ_1 show an initial decrease followed by an increase. Notably, there is a clear synchronization in the variations in λ_1 and μ_1 and the variations in λ_2 and μ_2, indicating that there is some coupling relationships in between λ_1 and μ_1 and between λ_2 and μ_2. From a mathematical perspective, this is a problem of related rates. Once the variation in ν with shear stress and bedding orientation is known, the corresponding δ can be derived, further reducing the difficulty of considering anisotropy in constructing the shear creep model.

Anisotropy is essentially related to the oriented microstructural arrangement within the rock, and the fabric tensor $\boldsymbol{F}'_{ij}$ can express anisotropic bodies under true stress as equivalent isotropic bodies under modified stress, thereby quantitatively describing the anisotropic mechanical behavior of bedded materials. Therefore, the fabric tensor can be used in constructing strength failure criterion or constitutive models for the anisotropic mechanical properties of bedded geomaterials (Pietruszczak and Mroz, 2000; Lu et al., 2021).

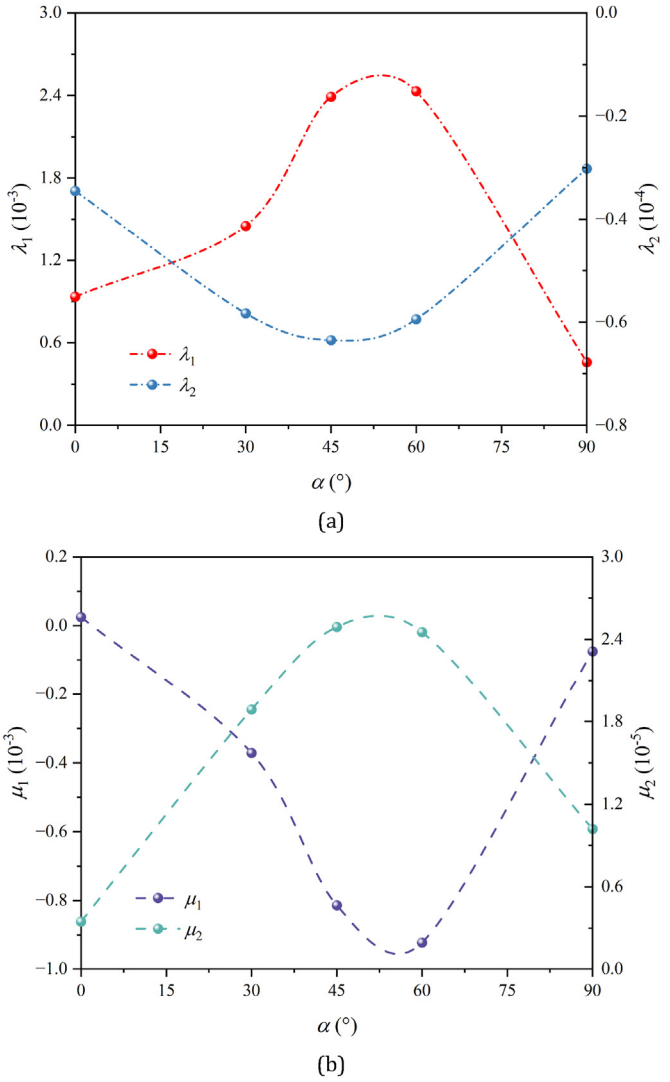

Fig. 17. Variations in parameters (a) λ_1 and λ_2, and (b) μ_1 and μ_2 with bedding inclination angle.

The stress state of shale specimens under the direct shear loading path is shown in Fig. 18a. The stress state of the specimens can be simplified into a normal component and a tangential stress traction vector in the two-dimensional (2D) stress field. Therefore, the direct shear creep test can be simplified into a 2D anisotropic mechanical problem; hence, the fabric tensor $\boldsymbol{F}'_{ij}$ can be constructed as follows:

$$\boldsymbol{F}'_{ij} = \frac{1}{2}\begin{bmatrix} 1+\Delta & 0 \\ 0 & 1-\Delta \end{bmatrix} \tag{17}$$

where Δ is the fabric parameter, which is used to quantitatively describe the degree of the initial anisotropy of the material.

As shown in Fig. 18b, the shear creep behavior of shale is primarily controlled by two stress components (shear stress and normal stress) and the bedding orientation. It assumes that shear and normal stresses are uniformly distributed on a shear failure surface. Therefore, for an element located at any point on a shear failure surface, the in-plane stress state during shear loading is represented by a combination of normal stress σ_n and shear stress τ components (see Fig. 18b). If the in-plane stress state is further expressed by the in-plane principal stress, it can be simplified to a compressive stress σ_1 and a tensile stress σ_2, as shown in Fig. 18c. Then, the angle θ between the normal direction of the bedding surface and the maximum in-plane principal stress σ_1 can be expressed as

$$\theta = \alpha - \frac{1}{2}\arctan(2\tau / \sigma_n) \tag{18}$$

When the principal stress direction is rotated relative to the material's principal axis, the fabric tensor should be transformed into a new fabric tensor determined by the principal stress direction in the reference coordinate system:

$$\boldsymbol{F}_{ij} = \boldsymbol{Q}_{ki}\boldsymbol{Q}_{lj}\boldsymbol{F}'_{ij} = \frac{1}{2}\begin{bmatrix} 1-\Delta\cos(2\theta) & \Delta\sin(2\theta) \\ \Delta\sin(2\theta) & 1+\Delta\cos(2\theta) \end{bmatrix} \quad (i,j = 1,2) \tag{19}$$

where $\boldsymbol{Q}$ is the conversion tensor formed by the cosine value of the angle between the direction of the fabric tensor and direction of the principal stress axis.

Furthermore, the deviatoric fabric tensor $\boldsymbol{F}^{\pi}_{ij}$ can be calculated by

$$\boldsymbol{F}^{\pi}_{ij} = \boldsymbol{F}_{ij} - \boldsymbol{F}_{kk}\delta_{ij}\Big/2 = \frac{\Delta}{2}\begin{bmatrix} -\cos(2\theta) & \sin(2\theta) \\ \sin(2\theta) & \cos(2\theta) \end{bmatrix} \tag{20}$$

where δ_{ij} is the Kronecker notation.

The in-plane stress tensor at a point on the shear failure surface can be expressed as follows:

$$\boldsymbol{\sigma}_{ij} = \begin{bmatrix} \sigma_n & \tau \\ \tau & 0 \end{bmatrix} \tag{21}$$

The corresponding deviatoric stress tensor can be expressed as follows:

$$\boldsymbol{s}_{ij} = \boldsymbol{\sigma}_{ij} - \boldsymbol{\sigma}_{kk}\delta_{ij}\Big/2 = \begin{bmatrix} \frac{\sigma_n}{2} & \tau \\ \tau & -\frac{\sigma_n}{2} \end{bmatrix} \tag{22}$$

At this point, the projection of the fabric tensor $\boldsymbol{F}_{ij}$ on the direction of the unit deviatoric stress tensor is an invariant, which can be defined as the anisotropic state variable ψ:

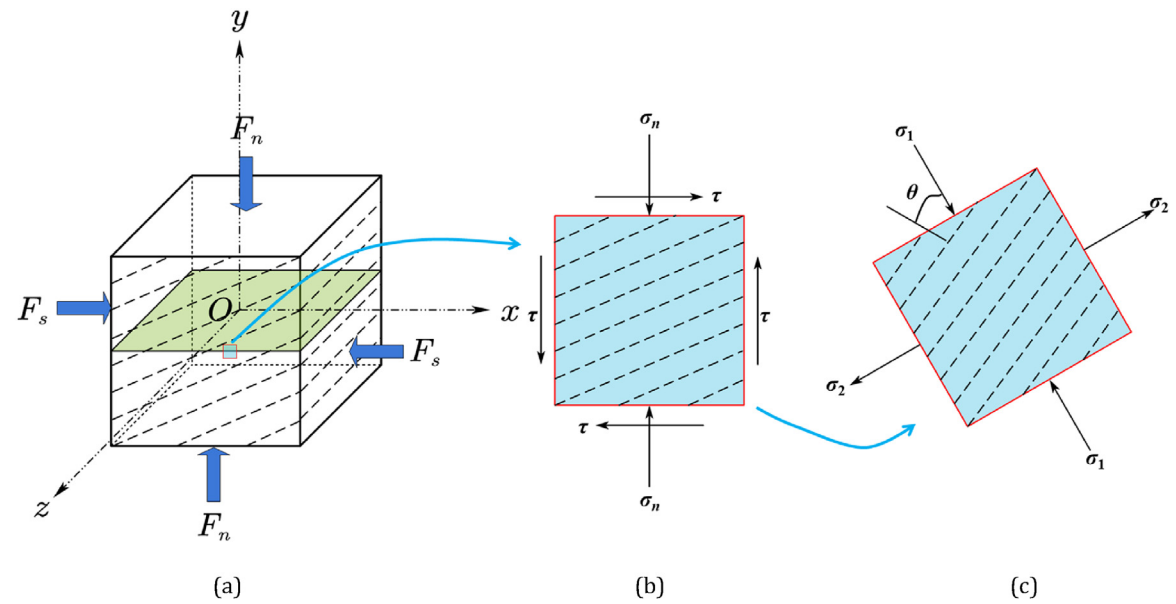

Fig. 18. (a) Stress state of the shale specimens during shear creep; (b) Stress state of any unit element on the shear failure surface; and (c) Stress state of the unit element represented by the in-plane principal stress state.

$$\psi = \boldsymbol{F}_{ij} : \boldsymbol{n}_{ij} = \boldsymbol{F}_{ij}^{\pi} : \boldsymbol{n}_{ij} = -\frac{\Delta}{2} \frac{1}{\sqrt{\frac{\sigma_n^2}{2} + 2\tau^2}} [\sigma_n \cos(2\theta) - 2\tau \sin(2\theta)] \tag{23}$$

where ψ can quantitatively characterize the intrinsic bedding anisotropy and stress-induced anisotropy in shear creep tests.

With the experimental results of shale anisotropic shear strength research (also see Fig. 17), it can be found that the change in material parameters μ_1 and μ_2 with bedding orientation is very similar to that of shear strength. This change is analogous to the Mohr–Coulomb strength criterion, which is widely used to describe the shear strength of geotechnical materials (Ishibashi et al., 2016):

$$\tau = c + f\sigma_n \tag{24}$$

where c is the cohesion and f is the friction coefficient.

Eqs. (24) and (16) are have a similar form (c is analogous to μ_1; f is analogous to μ_2). Referencing the construction method of the failure criterion of transversely isotropic geotechnical materials developed by Pietruszczak and Mroz (2000), the material parameters μ_1 and μ_2 can be written as functions of the anisotropic state variable ψ and are approximately given by the following equations:

$$\mu_1 = \mu_{11}\left(1 + \psi + \mu_{12}\psi^2 + \mu_{13}\psi^3\right) \tag{25}$$

$$\mu_2 = \mu_{21}\left(1 + \psi + \mu_{22}\psi^2 + \mu_{23}\psi^3\right) \tag{26}$$

where μ_{11}, μ_{12}, μ_{13}, μ_{21}, μ_{22} and μ_{23} are the independent constants.

By substituting Eqs. (25) and (26) into Eqs. (14)–(16), we can obtain a new shear anisotropic creep model of shale. However, the specific details of constructing the anisotropic shear creep model and comparing it with the experimental results need further studies.

5. Conclusions

In this study, creep tests of shale with five different bedding orientations (0°, 30°, 45°, 60°, and 90°) under multiple levels of direct shear stress were carried out. The anisotropic creep behavior of shale under the combined influence of weak bedding planes and direct shear loads was analyzed. Based on the experimental data on shear creep strain and creep rate, an improved logarithmic model was proposed. Finally, a new mathematical method for constructing anisotropic shear creep models was presented. The main conclusions of this paper are drawn as follows:

(1) The shear creep deformation of shale is predominantly viscoelastic under low shear stress levels. At all bedding inclination angles, the creep compliance of shale increases approximately linearly with the logarithmic increase in elapsed time, and the magnitude of the increase depends on the bedding orientation and the length of the creep time. The increment and rate of increase in the creep compliance of shale specimens with $\alpha = 0°$ are the largest after 4-h creeping.

(2) The anisotropic properties of shale creep compliance under high shear stress conditions show that the creep compliance at $\alpha = 0°$ is the minimum, followed by that at $\alpha = 90°$. With semilogarithmic and double-logarithmic coordinates, the overall slopes K_1 and K_2 of the creep compliance curve (ignoring the acceleration creep stage) show an increasing and then decreasing trend with the bedding orientation.

(3) The bedding inclination angle significantly controls the steady-state creep rate of shale under direct shear. At low shear stress levels, the steady-state creep rate at $\alpha = 0°$ is approximately ten times higher than at other bedding orientations. A semilogarithmic model is proposed that can simultaneously reflect the stress dependence of the steady-state creep rate and reveal the influence of bedding orientation on the steady-state creep rate, which limits the deviation of the calculated result from the observed steady-state creep rate.

(4) The power law, logarithmic, exponential, hyperbolic, and crack damage creep models all can approximately describe the evolution of creep strain with time, but only the power law and logarithmic models can fit the creep rate more effectively. In terms of long-term predictive ability, the power law model tends to "overestimate creep after loading durations," while the logarithmic model based on self-similar characteristics can give high-precision predictions. This indicates that the logarithmic model is acceptable for characterizing the anisotropic creep behavior of shale under direct shearing.

(5) A mathematical method for anisotropic shear creep model for shale is proposed, which takes into account the nonlinear dependence of the anisotropic creep behavior of shale under direct shear on shear stress and bedding orientation. The new methodology can significantly reduce the number of independent parameters and substantially reduce the computational burden. This is helpful in solving the anisotropic time-dependent problem of anisotropic geomaterials.

Data availability statement

All data, models, or code that support the findings of this study are available from the corresponding author upon reasonable request.

Declaration of competing interest

The authors declare that they have no known competing financial interests or personal relationships that could have appeared to influence the work reported in this paper.

Acknowledgments

This study was funded by the National Natural Science Foundation of China (Grant Nos. U22A20166 and 12172230), and the Guangdong Basic and Applied Basic Research Foundation (Grant No. 2023A1515012654). The authors would like to thank Dr. Yang Liu and Dr. Zhaopeng Zhang from the Key Laboratory of Deep Earth Science and Engineering (Ministry of Education) at Sichuan University for their useful discussions and experiment assistance in this work.

References

Baihly, J., Altman, R., Malpani, R., Luo, F., 2010. Shale gas production decline trend comparison over time and basins. In: The SPE Annual Technical Conference and Exhibition. Florence, Italy, September 2010, Paper Number: SPE-135555-MS.

Bažant, Z.P., Chern, J.C., 1983. Reply to Hilsdorf and Müller's discussion of "Comments on the use of Ross' hyperbola and recent comparisons of various practical creep prediction models". Cement Concr. Res. 13 (3), 444–448.

Bažant, Z.P., Chern, J.-C., 1984. Double-power logarithmic law for concrete creep. Cement Concr. Res. 14 (6), 793–806.

Bellani, J., Verma, H.K., Khatri, D., Makwana, D., Shah, M., 2021. Shale gas: a step toward sustainable energy future. J. Pet. Explor. Prod. Technol. 11 (5), 2127–2141.

Brantut, N., Heap, M.J., Meredith, P.G., Baud, P., 2013. Time-dependent cracking and brittle creep in crustal rocks: a review. J. Struct. Geol. 52, 17–43.

Brantut, N., Heap, M.J., Baud, P., Meredith, P.G., 2014. Mechanisms of time-dependent deformation in porous limestone. J. Geophys. Res. Solid Earth 119 (7), 5444–5463.

Carey, J.W., Lei, Z., Rougier, E., Mori, H., Viswanathan, H., 2015. Fracture-permeability behavior of shale. J. Unconv. Oil Gas Resour. 11, 27–43.

Chang, C., Zoback, M.D., 2009. Viscous creep in room-dried unconsolidated Gulf of Mexico shale (I): experimental results. J. Pet. Sci. Eng. 69 (3), 239–246.

Chau, V.T., Li, C., Rahimi-Aghdam, S., Bažant, Z.P., 2017. The enigma of large-scale permeability of gas shale: pre-existing or frac-induced? J. Appl. Mech. 84 (6), 061008.

De Schutter, G., 1999. Degree of hydration based Kelvin model for the basic creep of early age concrete. Mater. Struct. 32 (4), 260–265.

Du, J., Whittle, A.J., Hu, L., Divoux, T., Meegoda, J.N., 2021. Characterization of meso-scale mechanical properties of Longmaxi shale using grid microindentation experiments. J. Rock Mech. Geotech. Eng. 13 (3), 555–567.

Fan, Z.D., Xie, H.P., Zhang, R., Lu, H.J., Zhou, Q., Nie, X.F., Luo, Y., Ren, L., 2022. Characterization of anisotropic mode II fracture behaviors of a typical layered rock combining AE and DIC techniques. Eng. Fract. Mech. 271, 108599.

Geng, Z., Bonnelye, A., Chen, M., Jin, Y., Dick, P., David, C., Fang, X., Schubnel, A., 2017. Elastic anisotropy reversal during brittle creep in shale. Geophys. Res. Lett. 44 (21), 10, 887-10,895.

Geng, Z., Bonnelye, A., Chen, M., Jin, Y., Dick, P., David, C., Fang, X., Schubnel, A., 2018. Time and temperature dependent creep in tournemire shale. J. Geophys. Res. Solid Earth 123 (11), 9658–9675.

Guner, D., Golbasi, O., Ozturk, H., 2022. Generic creep behavior and creep modeling of an aged surface support liner under tension. J. Rock Mech. Geotech. Eng. 14 (2), 377–384.

Herrmann, J., Rybacki, E., Sone, H., Dresen, G., 2020. Deformation experiments on Bowland and Posidonia shale—part ii: creep behavior at in situ p_c–T conditions. Rock Mech. Rock Eng. 53 (2), 755–779.

Hilsdorf, H.K., Müller, H.S., 1983. A discussion of the note "Comments on the use of ross' hyperbola and recent comparisons of various practical creep prediction models" by Z. P. Bazant and J.C. Chern.Cem. Concr. Res. 13 (3), 441–443.

Ishibashi, T., Watanabe, N., Asanuma, H., Tsuchiya, N., 2016. Linking microearthquakes to fracture permeability change: the role of surface roughness. Geophys. Res. Lett. 43 (14), 7486–7493.

Kamali-Asl, A., Ghazanfari, E., 2017. Investigating the creep response of marcellus shale formations. In: Geotechnical Frontiers. Page, pp. 562–569.

Kong, L., Xie, H., Li, C., 2023. Coupled microplane and micromechanics model for describing the damage and plasticity evolution of quasi-brittle material. Int. J. Plast. 162, 103549.

Li, B., Yang, F., Du, P., Liu, Z., 2022. Study on the triaxial unloading creep mechanical properties and creep model of shale in different water content states. Bull. Eng. Geol. Environ. 81 (10), 420.

Li, C., Caner, F.C., Chau, V.T., Bažant, Z.P., 2017. Spherocylindrical microplane constitutive model for shale and other anisotropic rocks. J. Mech. Phys. Solid. 103, 155–178.

Li, C., Bažant, Z.P., Xie, H., Rahimi-Aghdam, S., 2019. Anisotropic microplane constitutive model for coupling creep and damage in layered geomaterials such as gas or oil shale. Int. J. Rock Mech. Min. Sci. 124, 104074.

Li, C., Wang, J., Xie, H., 2020. Anisotropic creep characteristics and mechanism of shale under elevated deviatoric stress. J. Pet. Sci. Eng. 185, 106670.

Li, C., Yang, D., Xie, H., Ren, L., Wang, J., 2023. Size effect of fracture characteristics for anisotropic quasi-brittle geomaterials. Int. J. Min. Sci. Technol. 33 (2), 201–213.

Liang, Z., Chen, Z., Rahman, S.S., 2020. Experimental investigation of the primary and secondary creep behaviour of shale gas reservoir rocks from deep sections of the Cooper Basin. J. Nat. Gas Sci. Eng. 73, 103044.

Liu, K., Jin, Z., Zeng, L., Ostadhassan, M., Xu, X., 2021a. Understanding the creep behavior of shale via nano-DMA method. Energy Rep. 7, 7478–7487.

Liu, K., Rassouli, F.S., Liu, B., Ostadhassan, M., 2021b. Creep behavior of shale: nanoindentation vs. triaxial creep tests. Rock Mech. Rock Eng. 54 (1), 321–335.

Lu, H.J., Xie, H.P., Luo, Y., Ren, L., Zhang, R., Li, C.B., Wang, J., Yang, M.Q., 2021. Failure characterization of Longmaxi shale under direct shear mode loadings. Int. J. Rock Mech. Min. Sci. 148, 104936.

McClure, M., Horne, R., 2014. Characterizing hydraulic fracturing with a tendency-for-shear-stimulation test. SPE Reservoir Eval. Eng. 17 (2), 233–243.

Mighani, S., Bernabé, Y., Boulenouar, A., Mok, U., Evans, B., 2019. Creep deformation in vaca muerta shale from nanoindentation to triaxial experiments. J. Geophys. Res. Solid Earth 124 (8), 7842–7868.

Naumenko, K., Altenbach, H., Gorash, Y., 2009. Creep analysis with a stress range dependent constitutive model. Arch. Appl. Mech. 79 (6), 619–630.

Palmer, I., Moschovidis, Z., Cameron, J., 2007. Modeling shear failure and stimulation of the barnett shale after hydraulic fracturing. In: The SPE Hydraulic Fracturing Technology Conference. College Station, Texas, U.S.A., January 2007. Paper Number: SPE-106113-MS.

Pietruszczak, S., Mroz, Z., 2000. Formulation of anisotropic failure criteria incorporating a microstructure tensor. Comput. Geotech. 26 (2), 105–112.

Rassouli, F.S., Zoback, M.D., 2018. Comparison of short-term and long-term creep experiments in shales and carbonates from unconventional gas reservoirs. Rock Mech. Rock Eng. 51 (7), 1995–2014.

Rybacki, E., Herrmann, J., Wirth, R., Dresen, G., 2017. Creep of Posidonia shale at elevated pressure and temperature. Rock Mech. Rock Eng. 50 (12), 3121–3140.

Shi, X., Jiang, S., Yang, L., Tang, M., Xiao, D., 2020. Modeling the viscoelasticity of shale by nanoindentation creep tests. Int. J. Rock Mech. Min. Sci. 127, 104210.

Slim, M., Abedi, S., Bryndzia, L.T., Ulm, F.-J., 2019. Role of organic matter on nano-scale and microscale creep properties of source rocks. J. Eng. Mech. 145 (1), 04018121.

Sone, H., Zoback, M.D., 2013a. Mechanical properties of shale-gas reservoir rocks — Part 1: static and dynamic elastic properties and anisotropy. Geophysics 78 (5), D381–D392.

Sone, H., Zoback, M.D., 2013b. Mechanical properties of shale-gas reservoir rocks — Part 2: ductile creep, brittle strength, and their relation to the elastic modulus. Geophysics 78 (5), D393–D402.

Sone, H., Zoback, M.D., 2014. Time-dependent deformation of shale gas reservoir rocks and its long-term effect on the in situ state of stress. Int. J. Rock Mech. Min. Sci. 69, 120–132.
Traore, S., Naik Parrikar, P., Mokhtari, M., 2022. Full-field creep mapping in a heterogeneous shale compared to a sandstone. Rock Mech. Rock Eng. 56 (1), 89–108.
Trzeciak, M., Sone, H., Dabrowski, M., 2018. Long-term creep tests and viscoelastic constitutive modeling of lower Paleozoic shales from the Baltic Basin, N Poland. Int. J. Rock Mech. Min. Sci. 112, 139–157.
Voltolini, M., 2021. In-situ 4D visualization and analysis of temperature-driven creep in an oil shale propped fracture. J. Pet. Sci. Eng. 200, 108375.
Wang, J., Yang, C., Liu, Y., Li, Y., Xiong, Y., 2022a. Using nanoindentation to characterize the mechanical and creep properties of shale: load and loading strain rate effects. ACS Omega 7 (16), 14317–14331.
Wang, P., Huang, H., Qu, Z., Wang, P.T., Han, Q., Ren, Z., 2022b. Creep experiments and theoretical research of shale hydration damage based on NMR. J. Dispersion Sci. Technol. 43 (13), 2002–2010.
Wang, Z., Gu, L., Zhang, Q., Yue, S., Zhang, G., 2020. Creep characteristics and prediction of creep failure of rock discontinuities under shearing conditions. Int. J. Earth Sci. 109 (3), 945–958.
Wilczynski, P.M., Domonik, A., Lukaszewski, P., 2021. Brittle creep and viscoelastic creep in lower Palaeozoic shales from the Baltic Basin, Poland. Energies 14 (15), 4633.
Yang, Y., Zoback, M., 2016. Viscoplastic deformation of the Bakken and adjacent formations and its relation to hydraulic fracture growth. Rock Mech. Rock Eng. 49 (2), 689–698.
Zhao, B., Liu, D., Dong, Q., 2011. Experimental research on creep behaviors of sandstone under uniaxial compressive and tensile stresses. J. Rock Mech. Geotech. Eng. 3, 438–444.
Zhao, J., Feng, X.-T., Zhang, X., Yang, C., Zhou, Y., 2018. Time-dependent behaviour and modeling of Jinping marble under true triaxial compression. Int. J. Rock Mech. Min. Sci. 110, 218–230.
Zhao, Y., Wang, Y., Wang, W., Wan, W., Tang, J., 2017. Modeling of non-linear rheological behavior of hard rock using triaxial rheological experiment. Int. J. Rock Mech. Min. Sci. 93, 66–75.

Cunbao Li received his BSc degree in Sichuan University in 2012, and PhD in Civil Engineering from the same University, in 2017, and postgraduate training in Northwestern University, China. He is currently working as an Assistant Professor at the Shenzhen University. His research interests focus on rock mechanics in deep earth and deep space.